

Cite this: *Nanoscale*, 2020, **12**, 4916

Band gap engineering of Ce-doped anatase TiO₂ through solid solubility mechanisms and new defect equilibria formalism†

Ghazaleh Bahmanrokh,^a Claudio Cazorla,^a Sajjad S. Mofarah,^a Reza Shahmiri,^a Yin Yao,^b Ismayadi Ismail,^c Wen-Fan Chen,^d Pramod Koshy^a and Charles Christopher Sorrell^a

The present work reports a detailed mechanistic interpretation of the role of the solubility of dopants and resultant midgap defect energies in band gap engineering. While there is a general perception that a single dopant is associated with single solubility and defect mechanisms, in reality, the potential for multiple solubility and defect mechanisms requires a more nuanced interpretation. Similarly, Kröger–Vink defect equilibria assume that stoichiometries during substitutional and interstitial solid solubility as well as Schottky and Frenkel pair formation are compensated by the diffusion of matrix ions to the grain boundaries or surface. However, this approach does not allow the possibility that stoichiometry is uncompensated, where diffusion of the matrix ion to lattice interstices occurs, followed by charge compensation by redox of this ion. Consequently, a modified defect equilibria formalism has been developed in order to allow description of this situation. Experimental data for the structural, chemical, semiconducting, and photocatalytic properties as a function of doping level are correlated with conceptual structural models, a comprehensive energy band diagram, and the corresponding defect equilibria. These correlations reveal the complex mechanisms of the interrelated solubility and defect formation mechanisms, which change significantly and irregularly as a function of small changes in doping level. The analyses confirm that the assumption of single mechanisms of solid solubility and defect formation may be simplifications of more complex processes. The generation of (1) a matrix of complementary characterisation and analytical data, (2) the calculation of a complete energy band diagram, (3) consideration of charge compensation mechanisms and redox beyond the limitations of Kröger–Vink approaches, and (4) the development of models of corresponding structural analogies combine to create a new approach to interpret and explain experimental data. These strategies allow deconstruction of these complex issues and thus targeting of optimal and possibly unique doping levels to achieve lattice configurations that may be energetically and structurally unfavorable. These approaches then can be applied to other doped semiconducting systems.

Received 7th October 2019,
Accepted 14th January 2020

DOI: 10.1039/c9nr08604h

rsc.li/nanoscale

1. Introduction

1.1 Photocatalytic TiO₂

Titanium dioxide (TiO₂, titania) is a semiconducting metal oxide that has been studied widely in response to its advantageous features, including photocatalytic properties, chemical stability, nontoxicity, availability, and cost.^{1,2,3–8} These pro-

erties have allowed it to find applications in many key technological areas including energy,^{9–16} natural environment,^{17–22} built environment,^{23–30} and biomedicine.^{31,32}

The photocatalytic activity of TiO₂ depends strongly on its properties, so many experimental studies and theoretical examinations have been done in order to investigate the effects of various parameters affecting the performance.^{33–35} The most important of these for anatase polymorph of TiO₂ are optical band gap^{36–41} (indirect band gap E_g of ~3.2 eV (ref. 36) and direct band gap E_g of ~3.5 eV), recombination time, recombination rate,^{36,42,43} diffusion distance,⁴⁴ electron mobility,^{34,51,52} quantum confinement,^{18,53–57} concentration of surface active sites,^{18,33,45} lattice stability,^{46–50} exposed crystallographic planes,^{51–56} and defect chemistry.^{57–60}

In nonstoichiometric TiO_{2–x}, the presence of intrinsic and extrinsic lattice defects can alter the Fermi energy level (E_f).⁶¹ The range of values determined for the E_f is illuminating

^aSchool of Materials Science and Engineering, UNSW Sydney, Sydney, NSW 2052, Australia. E-mail: g.bahmanrokh@unsw.edu.au

^bElectron Microscope Unit, Mark Wainwright Analytical Centre, UNSW Sydney, Sydney, NSW 2052, Australia

^cMaterials Synthesis and Characterization Laboratory, Institute of Advanced Technology (ITMA), Universiti Putra Malaysia, 43400 Serdang, Selangor, Malaysia

^dInstitute of Medical Science and Technology, National Sun Yat-sen University, Kaohsiung 80424, Taiwan

†Electronic supplementary information (ESI) available. See DOI: 10.1039/c9nr08604h

because these levels provide guidance for the processing and application of TiO₂ through the lowering of the E_f .⁶² This is critical because the relevant midgap defect energies should be above the E_f for n-type semiconductivity.⁶³ That is, the subshell energy levels above the E_f have a 50% chance of being unfilled and hence are more likely to be available to electrons while the energy levels below the E_f have a 50% chance of being filled and hence are more likely to be unavailable to electrons.⁶⁴

Since the anatase polymorph of TiO₂ is an n-type semiconductor,⁶⁵ then the free electron concentration in anatase is high and the E_f is close to the conduction band.^{61,66} While TiO₂ is used generically to describe the stoichiometry, oxygen vacancies ($V_O^{\bullet\bullet}$) are intrinsic defects in TiO₂.⁶⁷ Consequently, its stoichiometry is more correctly TiO_{2-x}, which is charge compensated by $Ti^{4+} \rightarrow Ti^{3+}$ redox,⁶⁸ where there are two such reduction reactions for each oxygen vacancy. While Ti^{3+} and $V_O^{\bullet\bullet}$ are intrinsic to TiO_{2-x}, processing under low oxygen partial pressures (P_{O_2}) also can generate titanium vacancies ($V_{Ti}^{\prime\prime\prime}$).⁶⁹ All three of these defects are responsible for the formation of midgap states, which may be able to reduce the band gap. Intrinsic defects in the form of Ti vacancies and oxygen vacancies as well as extrinsic donor and acceptor defects resulting from doping are used commonly in attempts to improve the semiconducting properties generally through band gap reduction by lowering the conduction band, raising the valence band, and/or introducing midgap states.⁷⁰ These defects can act as electron and hole traps, which can increase the recombination times and alter the recombination rates.^{42,43}

1.2 Modification of TiO₂

Despite the potential advantages offered by anatase in applications for energy and the environment, its photocatalytic performance is suboptimal largely because it is a wide band gap semiconductor,³⁶ so it absorbs radiation largely only in the ultraviolet range,⁷¹ which represents only 3–5% of the solar spectrum.⁷² It is well established that semiconducting properties can be enhanced through doping, with the aim of narrowing the E_g and thus shifting the absorption edge toward the visible part of the spectrum.^{73,74} Consequently, there have been many studies reporting data for the outcomes of doping by transition metals,^{75,76} rare earth metals,^{1,77,78} noble metals^{79–82} and nonmetals.^{83–85} The purpose of these strategies generally is to reduce the E_g by lowering the conduction band (CB), raising the valence band (VB), and/or introducing midgap energy levels.^{86,87} The 3d transition metals and, to lesser extents, the 4d and 5d transition metals have been studied as dopants numerous times owing to the proximity of these energy levels to those of the Ce 4f,^{88,89} their effects have shown inconsistent trends in performance outcomes.^{74–76,88,89} However, 4f rare earth ion dopants possibly offer more consistent outcomes owing to their differences in electron orbital shapes and orientation but also the greater proximity of their energy levels.

Relative to transition metal dopants, these factors have resulted in the observation of high photocatalytic activities, extension of the photoresponse range to the visible region,⁸⁸

and improvement in the separation of electron–hole pairs (excitons) and associated reduction in the recombination time.^{76,90}

Cerium as a dopant is unusual in that it exhibits ready $Ce^{4+} \leftrightarrow Ce^{3+}$ redox switching.⁷⁶ The ability to manipulate this through doping, atmospheric, or environmental effects is advantageous because it can: (1) alter the band positions favourably, (2) facilitate the solubility of dopants of valence 3+ and 4+, (3) increase the number and type of surface-active sites, (4) enhance recrystallisation, and (5) suppress grain growth.^{18,33,39,45} Consequently, Ce-doped TiO₂ has been studied numerous times, as shown by the comprehensive survey of previous work in Table I (see ESI†).

The CeO₂–TiO₂ phase diagram does not appear to have been determined, so an assessment of the potential for solubility of Ce in the TiO₂ lattice is not available. According to Hume-Rothery's rules for substitutional metallic solid solubility,⁹¹ it is unlikely that, as given in Table 1, the large Ce^{4+} (0.1010 nm) and Ce^{3+} (0.1150 nm) ions would substitute for the smaller Ti^{4+} (0.0745 nm) and Ti^{3+} (0.081 nm) ions in sixfold coordination.⁹² However, anatase does not exhibit ideal TiO₆ octahedral symmetry because the c axis of the octahedron is elongated and contains two large adjacent interstices of radii 0.0782 nm,³³ as given Table 1. These interstices also appear to be unlikely to be able to accommodate the large Ce ion above or below the central Ti ion and so Hume-Rothery's rules for interstitial metallic solid solubility⁹¹ indicate that this solubility mechanism also is unlikely. However, recently, the concept of *integrated solid solubility* has been introduced,⁸⁹ which involves solubility of the Ce ion on the combined sites of the central Ti^{4+} ion and an adjacent interstice (0.1527 nm sum), which is sufficiently large to accommodate both Ce valences.

In the CeO₂–TiO₂ system, once the solubility limit for CeO₂ in TiO₂ is reached under oxidising conditions, CeO₂ will precipitate.⁹³ However, under reducing conditions, two photocatalytic intermediate phases can form. The first to precipitate would be Ce₂O₃·4TiO₂³⁸ and, at Ce molar concentrations >33%, Ce₂O₃·2TiO₂⁹³ would form. However, in general, dopant

Table 1 Crystal radii of Ti and Ce ions

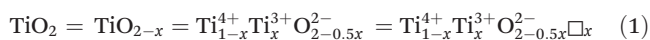
Ion	Co-ordination	Crystal radius (nm)	Difference with Ti^{4+} (%)	Difference with interstice (%)
Ti^{3+}	VI	0.0810	+8.7	+3.6
	V	(0.0704) ^a	+8.3	–10.0
Ti^{4+}	VI	0.0745	—	–5.0
	V	0.0650	—	–16.9
Ce^{3+}	VI	0.115	+54.4	+47.1
	V	(0.100) ^a	+34.2	+27.9
Ce^{4+}	VI	0.101	+35.6	+29.2
	V	(0.088) ^a	+18.1	+12.5
O^{2-}	III	0.122	+63.8	+56.0
Interstice	V	0.0782	—	—

^a Data not available but estimated from Ti(v)/Ti(vi) ratio

levels are held to relatively low levels of <1 mol% because over-doping effectively increases the band gap⁹⁴ and a high density of trapping sites increases the potential for multiple trapping of the individual charge carriers, thereby reducing the mobilities.⁷¹

1.3 TiO₂ defect equilibria

The effect of oxygen activity on the concentration of both ionic and electronic defects can be examined through the defect equilibria. Most oxide ceramic semiconductors exhibit oxygen deficiency, *e.g.*, CeO_{2-x} and TiO_{2-x}. This nonstoichiometry results in formation of defects such as ion vacancies or interstitials and compensating charged defects by either ionic compensation or electronic compensation. A second alternative charge-compensation mechanism is redox, which for TiO_{2-x} involves Ti⁴⁺ ↔ Ti³⁺ and is as follows:



where □ is an oxygen vacancy.

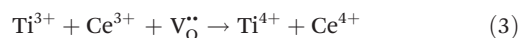
In addition to redox in the TiO_{2-x} matrix, a third charge-compensation mechanism is for matrix and dopant ions through intervalence charge transfer (IVCT):^{33,68,89,91}



The X-ray photoelectron spectroscopy (XPS) data presented subsequently confirm that the precursor valence of Ti⁴⁺ and Ce³⁺ partially alter to Ti³⁺ and Ce⁴⁺, which supports this mechanism.

It is counter-intuitive to conclude that annealing in air would be likely to retain Ce³⁺ and Ti³⁺ in their reduced states. However, XPS data of the present work and those of others⁹⁵ demonstrate the simultaneous presence of both oxidised and reduced valences. This potentially can be explained by a fourth charge-compensation mechanism, which is the effect of electronegativity, the range of values of which is given in Table 2. In the first instance, for the elemental electronegativities, the electrons would be pulled toward Ti, not Ce. In the second instance, the data of Smith,⁹⁶ which uniquely include valence, Ti³⁺ and Ce⁴⁺ (right side of eqn (2)) have identical electronegativities, which would not favour mutual charge transfer, but Ti⁴⁺ and Ce³⁺ (left side of eqn (2)) would favour charge transfer by increasing the effective valence of Ti⁴⁺ and decreasing the effective valence of Ce³⁺. As will be shown with the XPS data, the converse of these two effects was observed, suggesting that electronegativity is unlikely to be a charge-compensation mechanism.

A fifth charge-compensation mechanism is simply oxidation resulting from the interaction of Ce³⁺ and Ti³⁺ precursors with V_O^{••} according to the reaction:^{33,68}



This mechanism cannot be assessed because annealing in air at would be likely to cause direct oxidation to form the thermodynamically stable valences Ce⁴⁺ and Ti⁴⁺,^{91,97} so the two oxidation mechanisms cannot be decoupled. The relevance of these five potential charge-compensation mechanisms generally can be assessed with relative confidence by examination of the peak shifts in the XPS data, which indicate valence changes from the stoichiometric condition.

More generally, it is assumed commonly that doping results in substitution, generally on the cation sublattice. Substitutional Ce doping in TiO_{2-x} could induce shallow energy levels owing to the proximity of the unoccupied Ce 4f states ([Xe] 4f¹ 5d¹ 6s²; for *n* = 4f, *E* = -0.85 eV) and Ti 3d states ([Ar] 3d² 4s²; for *n* = 3d, *E* = -1.51 eV), so this rare earth cation offers the potential to enhance the photocatalytic activity,⁹⁸ although other factors may dominate the performance such that it is degraded.

Following from a comprehensive survey of previous studies of Ce-doped TiO₂, the present work considers the solubility and defect formation mechanisms based on a complete doping study of thin films of Ce-doped anatase synthesised by sol-gel and annealed at 450 °C for 2 h on fused SiO₂ and Si (110) substrates. These conditions yielded the maximal crystallinity over the range 350°–650 °C. The mechanistic interpretation of the phenomena is based on a consistent set of data obtained from XRD, Raman, AFM, TEM-EDS, XPS (surface and valence band), UV-Vis (absorption and transmission), AM-KPFM, and photocatalytic performance; these were supplemented with comprehensive DFT modelling of the energy band diagram.

The interpretation of the preceding is based on a consistent set of correlations between the experimental data, the development of structural models for the different solubility mechanisms, and consideration of a complete defect energy diagram with all potential defect energy levels using a modified defect equilibria formalism that has been developed in order to accommodate an alternative charge-compensation mechanism (Ti⁴⁺ ↔ Ti³⁺ redox) based on the Kröger-Vink assumption of composition-compensated stoichiometry. The rationale for the present work is to derive a comprehensive mechanistic interpretation of the governing physical phenomena based on the solubility mechanisms and defect equilibria revealed by the complex outcomes of a precise doping study of cerium in anatase.

Table 2 Summary of electronegativities of Ti and Ce in different scales

Scale	Smith	Allen	Allred-Rochow	Little, Jr.	Mulliken	Pauling	Pearson	Sanderson	Nagle
Ref.	96	99	100	101	102 and 103	104	105	106 and 107	108
Ti ³⁺	1.50	1.38	1.32	1.32	5.20	1.54	3.45	1.50	—
Ti ⁴⁺	1.65	—	—	—	—	—	—	—	—
Ce ³⁺	1.15	—	1.08	—	1.80	1.12	—	1.34	1.05
Ce ⁴⁺	1.50	—	—	—	—	—	—	—	—

Consequently, the present work introduces a number of new concepts to the field of band gap engineering:

(1) Comprehensive doping study of TiO₂, from undoped to overdoped, incorporating fundamental concepts of solubility mechanisms, structural analogies, defect equilibria, midgap defect states, and Fermi levels.

(2) The first complete intrinsic and extrinsic defect energy level diagram for TiO₂.

(3) Correlation of a wide range of experimental mineralogical, nanostructural, structural, chemical, optical, semiconducting, and photocatalytic data with the preceding data.

(4) Modified defect equilibria formalism that overcomes the limitations of Kröger-Vink assumptions, thereby allowing the potential for uncompensated stoichiometry and charge compensation by redox.

2. Experimental procedure

See ESI† for details of experiments and density functional theory (DFT) calculations.

3. Results

3.1 Modified defect equilibria formalism

The defect equilibria are described by Kröger-Vink notation¹⁰⁹ for both types of solid solubility and charge compensation as well as for both valences of matrix (Ti³⁺, Ti⁴⁺) and dopant (Ce³⁺, Ce⁴⁺). However, this system assumes that stoichiometry is retained (*viz.*, compensated) upon doping and so the ionic ratios remain constant as given in left column in Table 3.

Table 3 Defect equilibria for both types of solid solubility and charge compensated stoichiometry and uncompensated stoichiometry for both valences of matrix (Ti³⁺, Ti⁴⁺) and dopant (Ce³⁺, Ce⁴⁺)

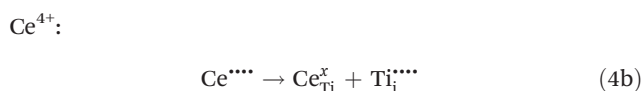
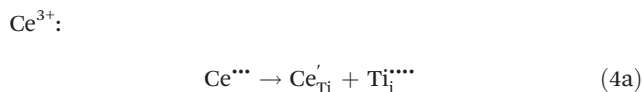
	Compensated stoichiometry	Uncompensated stoichiometry	
Substitutional solid solubility	Ionic compensation	Ionic compensation	
	$\text{Ce}_2\text{O}_3 \xrightarrow{2\text{TiO}_2} 2\text{Ce}'_{\text{Ti}} + \text{V}''_{\text{O}} + 3\text{O}^{\times}_{\text{O}}$	$2\text{Ce}^{\bullet\bullet\bullet} \xrightarrow{2\text{TiO}_2} 2\text{Ce}'_{\text{Ti}} + 2\text{Ti}_i^{\bullet\bullet\bullet} + 3\text{O}^{\times}_{\text{O}} + 6\text{Ti}'_{\text{Ti}-1}$	
	$\text{CeO}_2 \xrightarrow{\text{TiO}_2} \text{Ce}^{\times}_{\text{Ti}} + 2\text{O}^{\times}_{\text{O}}$	$\text{CeO}_2 \xrightarrow{\text{TiO}_2} \text{Ce}^{\times}_{\text{Ti}} + 2\text{O}^{\times}_{\text{O}}$	
	$\text{Ce}_2\text{O}_3 \xrightarrow{\text{Ti}_2\text{O}_3} 2\text{Ce}^{\times}_{\text{Ti}} + 3\text{O}^{\times}_{\text{O}}$	$2\text{Ce}^{\bullet\bullet\bullet} \xrightarrow{\text{Ti}_2\text{O}_3 (\text{TiO}_2)} 2\text{Ce}^{\times}_{\text{Ti}} + 2\text{Ti}_i^{\bullet\bullet\bullet} + 3\text{O}^{\times}_{\text{O}} + 6\text{Ti}'_{\text{Ti}-1}$	
	$4\text{CeO}_2 \xrightarrow{2\text{Ti}_2\text{O}_3} 4\text{Ce}^{\times}_{\text{Ti}} + 8\text{O}^{\times}_{\text{O}} + \text{V}''''_{\text{Ti}}$	$2\text{Ce}^{\bullet\bullet\bullet} \xrightarrow{\text{Ti}_2\text{O}_3 (\text{TiO}_2)} 2\text{Ce}^{\times}_{\text{Ti}} + 2\text{Ti}_i^{\bullet\bullet\bullet} + 4\text{O}^{\times}_{\text{O}} + 8\text{Ti}'_{\text{Ti}-1}$	
	Electronic compensation	Electronic compensation	
	$\text{Ce}_2\text{O}_3 + 1/2\text{O}_2 (\text{g}) \xrightarrow{2\text{TiO}_2} 2\text{Ce}'_{\text{Ti}} + 4\text{O}^{\times}_{\text{O}} + 2\text{h}^{\bullet}$	$\text{Ce}^{\bullet\bullet\bullet} \xrightarrow{\text{TiO}_2} \text{Ce}'_{\text{Ti}} + \text{Ti}_i^{\bullet\bullet\bullet} + 2\text{O}^{\times}_{\text{O}} + 3\text{e}'$	
	$\text{CeO}_2 \xrightarrow{\text{TiO}_2} \text{Ce}^{\times}_{\text{Ti}} + 2\text{O}^{\times}_{\text{O}}$	$\text{Ce}^{\bullet\bullet\bullet} \xrightarrow{\text{TiO}_2} \text{Ce}^{\times}_{\text{Ti}} + \text{Ti}_i^{\bullet\bullet\bullet} + 2\text{O}^{\times}_{\text{O}} + 4\text{e}'$	
	$\text{Ce}_2\text{O}_3 \xrightarrow{\text{Ti}_2\text{O}_3} 2\text{Ce}^{\times}_{\text{Ti}} + 3\text{O}^{\times}_{\text{O}}$	$2\text{Ce}^{\bullet\bullet\bullet} \xrightarrow{\text{Ti}_2\text{O}_3 (\text{TiO}_2)} 2\text{Ce}^{\times}_{\text{Ti}} + 2\text{Ti}_i^{\bullet\bullet\bullet} + 3\text{O}^{\times}_{\text{O}} + 6\text{e}'$	
	$2\text{CeO}_2 + \text{V}''_{\text{O}} \xrightarrow{\text{Ti}_2\text{O}_3} 2\text{Ce}^{\times}_{\text{Ti}} + 3\text{O}^{\times}_{\text{O}}$	$2\text{Ce}^{\bullet\bullet\bullet} \xrightarrow{\text{Ti}_2\text{O}_3 (\text{TiO}_2)} 2\text{Ce}^{\times}_{\text{Ti}} + 2\text{Ti}_i^{\bullet\bullet\bullet} + 3\text{O}^{\times}_{\text{O}} + 8\text{e}'$	
	Interstitial solid solubility	Ionic compensation	Ionic compensation
		$2\text{Ce}_2\text{O}_3 \xrightarrow{4\text{TiO}_2} 4\text{Ce}_i^{\bullet\bullet\bullet} + 3\text{V}''''_{\text{Ti}} + 6\text{O}^{\times}_{\text{O}}$	$2\text{Ce}^{\bullet\bullet\bullet} \xrightarrow{2\text{TiO}_2} 2\text{Ce}_i^{\bullet\bullet\bullet} + 3\text{O}^{\times}_{\text{O}} + 6\text{Ti}'_{\text{Ti}-1}$
		$\text{CeO}_2 \xrightarrow{\text{TiO}_2} \text{Ce}_i^{\bullet\bullet\bullet} + \text{V}''''_{\text{Ti}} + 2\text{O}^{\times}_{\text{O}}$	$\text{Ce}^{\bullet\bullet\bullet} \xrightarrow{\text{TiO}_2} \text{Ce}_i^{\bullet\bullet\bullet} + 2\text{O}^{\times}_{\text{O}} + 4\text{Ti}'_{\text{Ti}-1}$
		$\text{Ce}_2\text{O}_3 \xrightarrow{\text{Ti}_2\text{O}_3} 2\text{Ce}_i^{\bullet\bullet\bullet} + 2\text{V}''''_{\text{Ti}} + 3\text{O}^{\times}_{\text{O}}$	$\text{Ce}^{\bullet\bullet\bullet} \xrightarrow{\text{TiO}_2} \text{Ce}_i^{\bullet\bullet\bullet} + 2\text{O}^{\times}_{\text{O}} + \text{Ce}'_{\text{Ce}-1} + 2\text{Ti}'_{\text{Ti}-1}$
$6\text{CeO}_2 \xrightarrow{3\text{Ti}_2\text{O}_3} 6\text{Ce}_i^{\bullet\bullet\bullet} + 8\text{V}''''_{\text{Ti}} + 12\text{O}^{\times}_{\text{O}}$		$2\text{Ce}^{\bullet\bullet\bullet} \xrightarrow{\text{Ti}_2\text{O}_3 (\text{TiO}_2)} 2\text{Ce}_i^{\bullet\bullet\bullet} + 3\text{O}^{\times}_{\text{O}} + 6\text{Ti}'_{\text{Ti}-1}$	
Electronic compensation		Electronic compensation	
$\text{Ce}_2\text{O}_3 + 1/2\text{O}_2 (\text{g}) \xrightarrow{2\text{TiO}_2} 2\text{Ce}_i^{\bullet\bullet\bullet} + 4\text{O}^{\times}_{\text{O}} + 6\text{e}'$		$\text{Ce}^{\bullet\bullet\bullet} \xrightarrow{\text{TiO}_2} \text{Ce}_i^{\bullet\bullet\bullet} + 2\text{O}^{\times}_{\text{O}} + 3\text{e}'$	
$\text{CeO}_2 \xrightarrow{\text{TiO}_2} \text{Ce}_i^{\bullet\bullet\bullet} + 2\text{O}^{\times}_{\text{O}} + 4\text{e}'$		$\text{Ce}^{\bullet\bullet\bullet} \xrightarrow{\text{TiO}_2} \text{Ce}_i^{\bullet\bullet\bullet} + 2\text{O}^{\times}_{\text{O}} + 4\text{e}'$	
$\text{Ce}_2\text{O}_3 \xrightarrow{\text{Ti}_2\text{O}_3} 2\text{Ce}_i^{\bullet\bullet\bullet} + 3\text{O}^{\times}_{\text{O}} + 6\text{e}'$		$\text{Ce}^{\bullet\bullet\bullet} \xrightarrow{\text{TiO}_2} \text{Ce}_i^{\bullet\bullet\bullet} + 2\text{O}^{\times}_{\text{O}} + \text{Ce}'_{\text{Ce}-1} + 2\text{e}'$	
$2\text{CeO}_2 + \text{V}''_{\text{O}} \xrightarrow{\text{Ti}_2\text{O}_3} 2\text{Ce}_i^{\bullet\bullet\bullet} + 3\text{O}^{\times}_{\text{O}} + 6\text{e}'$		$2\text{Ce}^{\bullet\bullet\bullet} \xrightarrow{\text{Ti}_2\text{O}_3 (\text{TiO}_2)} 2\text{Ce}_i^{\bullet\bullet\bullet} + 3\text{O}^{\times}_{\text{O}} + 6\text{e}'$	
		$2\text{Ce}^{\bullet\bullet\bullet} \xrightarrow{\text{Ti}_2\text{O}_3 (\text{TiO}_2)} 2\text{Ce}_i^{\bullet\bullet\bullet} + 3\text{O}^{\times}_{\text{O}} + 8\text{e}'$	
		$2\text{Ce}^{\bullet\bullet\bullet} \xrightarrow{\text{Ti}_2\text{O}_3 (\text{TiO}_2)} 2\text{Ce}_i^{\bullet\bullet\bullet} + 3\text{O}^{\times}_{\text{O}} + 2\text{Ce}'_{\text{Ce}-1} + 4\text{Ti}'_{\text{Ti}-1}$	
		Electronic compensation	
		$\text{Ce}^{\bullet\bullet\bullet} \xrightarrow{\text{TiO}_2} \text{Ce}_i^{\bullet\bullet\bullet} + 2\text{O}^{\times}_{\text{O}} + 3\text{e}'$	
	$\text{Ce}^{\bullet\bullet\bullet} \xrightarrow{\text{TiO}_2} \text{Ce}_i^{\bullet\bullet\bullet} + 2\text{O}^{\times}_{\text{O}} + 4\text{e}'$		
	$\text{Ce}^{\bullet\bullet\bullet} \xrightarrow{\text{TiO}_2} \text{Ce}_i^{\bullet\bullet\bullet} + 2\text{O}^{\times}_{\text{O}} + \text{Ce}'_{\text{Ce}-1} + 2\text{e}'$		
	$2\text{Ce}^{\bullet\bullet\bullet} \xrightarrow{\text{Ti}_2\text{O}_3 (\text{TiO}_2)} 2\text{Ce}_i^{\bullet\bullet\bullet} + 3\text{O}^{\times}_{\text{O}} + 6\text{e}'$		
	$2\text{Ce}^{\bullet\bullet\bullet} \xrightarrow{\text{Ti}_2\text{O}_3 (\text{TiO}_2)} 2\text{Ce}_i^{\bullet\bullet\bullet} + 3\text{O}^{\times}_{\text{O}} + 8\text{e}'$		
	$2\text{Ce}^{\bullet\bullet\bullet} \xrightarrow{\text{Ti}_2\text{O}_3 (\text{TiO}_2)} 2\text{Ce}_i^{\bullet\bullet\bullet} + 3\text{O}^{\times}_{\text{O}} + 2\text{Ce}'_{\text{Ce}-1} + 4\text{e}'$		

Ce'_{Ti} = Ce³⁺ substituting on Ti⁴⁺ site (single negative charge). Ce_{Ti}^x = Ce⁴⁺ substituting on Ti⁴⁺ site (no net charge). Ce_{Ti}[•] = Ce⁴⁺ substituting on Ti³⁺ site (single positive charge). Ce_i^{•••} = Ce³⁺ interstitial (triple positive charge). Ce_i^{••••} = Ce⁴⁺ interstitial (quadruple positive charge). Ti_i^{•••} = Ti³⁺ interstitial (triple positive charge). Ti_i^{••••} = Ti⁴⁺ interstitial (quadruple positive charge). Ce'_{Ce-1} = Ce⁴⁺ → Ce³⁺ reduction of Ce⁴⁺ interstitial (single negative charge). Ce_{Ce-1}[•] = Ce³⁺ → Ce⁴⁺ oxidation of Ce³⁺ interstitial (single positive charge). Ce'_{Ce-1} = Ce⁴⁺ → Ce³⁺ reduction of Ce⁴⁺ on lattice Ti site (single negative charge). Ce_{Ce-1}[•] = Ce³⁺ → Ce⁴⁺ oxidation of Ce³⁺ on lattice Ti site (single positive charge). Ti'_{Ti-1} = Ti⁴⁺ → Ti³⁺ reduction of interstitial Ti⁴⁺ (single negative charge). Ti_{Ti-1}[•] = Ti³⁺ → Ti⁴⁺ oxidation of interstitial Ti³⁺ (single positive charge). Ti'_{Ti-1} = Ti⁴⁺ → Ti³⁺ reduction of lattice Ti⁴⁺ (single negative charge). Ti_{Ti-1}[•] = Ti³⁺ → Ti⁴⁺ oxidation of lattice Ti³⁺ (single positive charge). O_O^x = Oxygen on lattice oxygen site (no net charge). O₂(g) = Oxygen gas (no net charge). V_{Ti}^{•••} = Ti³⁺ vacancy (triple negative charge). V_{Ti}^{••••} = Ti⁴⁺ vacancy (quadruple negative charge). V_O^{••} = O₂⁻ vacancy (double positive charge). e' = Electron (single negative charge). h[•] = Electron hole (single positive charge).

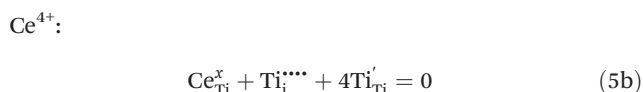
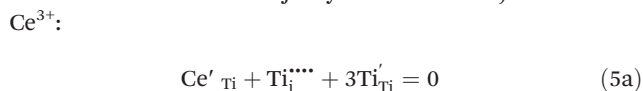
Although Kröger–Vink notation¹⁰⁹ is used very commonly to describe defect equilibria, in reality, they risk being inapplicable because most studies^{86,97,110–118} involve stoichiometrically *uncompensated* additions of dopant, which Kröger–Vink notation¹⁰⁹ would require any excess matrix cations to migrate to the surface. However, with TiO₂, the presence of two large interstices adjacent to the central Ti lattice site⁶⁸ suggests that, upon substitution by Ce, it would be energetically more favourable for Ti ions to move to one of these interstices rather than diffuse to the surface. The potential for integrated solid solubility⁸⁹ would facilitate strain and energy minimisation. Consequently, a new formalism for defect equilibria for uncompensated stoichiometry is given in order to accommodate this possibility.

In this formalism for a TiO_{2-x} matrix consisting of majority Ti⁴⁺ and minority Ti³⁺ (represented as TiO₂ and Ti₂O₃, respectively), there are two principal criteria for charge balance in the case of substitutional solid solubility:

(1) When Ce substitutes for majority Ti, it creates an adjacent Ti interstitial in 1 : 1 ratio:



(2) The Ce substitutional and adjacent Ti interstitial are charge compensated by reduction of neighbouring Ti⁴⁺ on lattice sites (or of the Ti interstitial) to Ti³⁺ (with matrix indicated as Ti₂O₃ (TiO₂) when Ce⁴⁺ substitutes for minority Ti³⁺ but redox still occurs at a majority Ti⁴⁺ lattice site):



The feasibility for charge compensation by Ti redox is supported by the relevant redox potentials given in Table 4. These data show that Ti⁴⁺ ↔ Ti³⁺ redox equilibria are facilitated by a

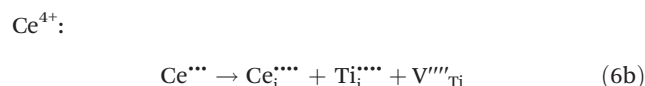
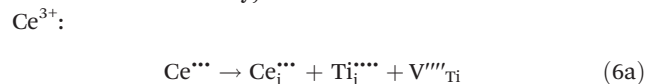
Table 4 Relevant redox potentials for Ti and Ce

Reaction	Redox reaction Ti ⁴⁺ + e ⁻ → Ti ³⁺	Potential (eV)	Ref.
1		+0.06	119
		0.00	120
		-0.09	120 (IV-III) ^a
2	Ti ⁴⁺ + 2e ⁻ → Ti ²⁺	-0.37	119 and 120
3	Ti ³⁺ + e ⁻ → Ti ²⁺	-0.90	120, 121 and 122
		-0.60	123
		-0.37	123
4	Ce ⁴⁺ + e ⁻ → Ce ³⁺	+1.72	121 and 122
		+1.61	120
		+1.44	124
5	Ce ⁴⁺ + 2e ⁻ → Ce ²⁺	+3.26	Present work
6	Ce ³⁺ + e ⁻ → Ce ²⁺	+1.67	125

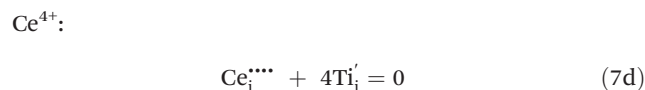
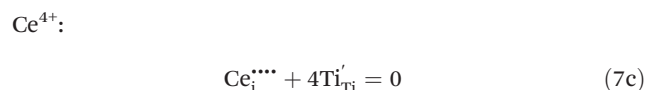
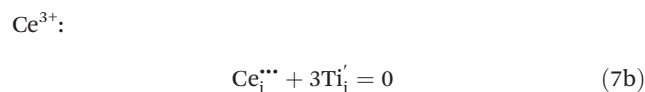
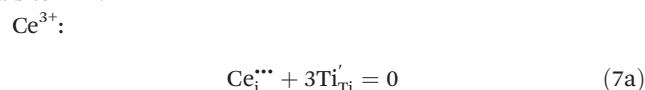
^aTi(III) = Ti bonded to, e.g., OH: Ti(OH)₃ Ti(OH)₂⁺ Ti(OH)₂²⁺

near-zero redox potential while all other potential charge-compensating redox equilibria for both Ti and Ce are significantly higher and hence unlikely. The principal criteria for charge balance in the case of interstitial solid solubility are:

(1) When a Ce³⁺ interstitial forms, it occupies one of the two interstices along the *c* axis, adjacent to the central majority Ti⁴⁺ lattice site. Ce³⁺–Ti⁴⁺ repulsion would transpose the Ti⁴⁺ ion into the other interstice, thereby creating a Frenkel pair (Ti interstitial and Ti vacancy):



(2) The Ce interstitial again is charge compensated by reduction of neighbouring Ti⁴⁺ on lattice sites or of Ti interstitials to Ti³⁺:



The new formalism for defect equilibria for uncompensated stoichiometry, where the ionic ratios do not remain constant, are as given in the right column of Table 3.

3.2 Midgap energy states

Contrasting the Kröger–Vink defect equilibria¹⁰⁹ with those of the new formalism, it can be seen that the interpretation of the effects of the midgap states deriving from these defects is entirely different. For example, assuming compensated stoichiometry, the midgap states arising from ionically compensated Ce⁴⁺ substitution for Ti³⁺ (eqn (11)) would be expected to be associated with 4Ce_{Ti}[•] and V_{Ti}^{••••} (self-charge-compensated). In contrast, with uncompensated stoichiometry (eqn (27)), these midgap states would be assumed to be 2Ce_{Ti}[•] and 2Ti_i^{••} (8 × Ti⁴⁺ → Ti³⁺ redox-charge-compensated).

The relevance of these considerations is shown in Fig. 1, which gives the energy levels for all of the possible defects (*i.e.*, defect energy levels) in Ce-doped TiO_{2-x} (anatase), including those calculated by others^{58,126,128,132} and by spin-polarised DFT in the present work (Ce_{Ti}[•], Ce_{Ti}^{••}, Ce_{Ti}^x [4+ and 3+], Ce_i^{••••}, Ce_i^{••}, Ce_i[•]). It can be seen that there are many potential midgap states formed within the band gap near the CB or VB or in the centre of the band gap. These can be intrinsic, such as Ti³⁺ and V_O^{••}, or extrinsic and so induced by Ce doping, such

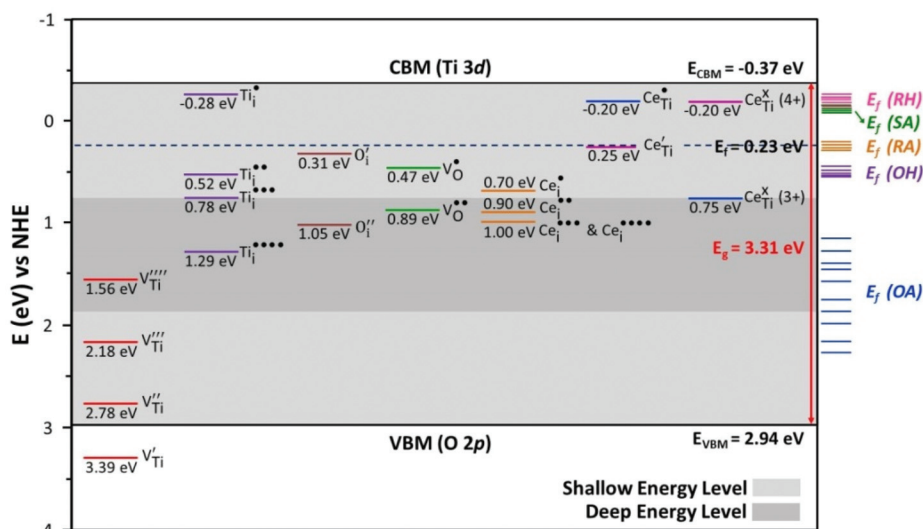


Fig. 1 Comprehensive defect energy level diagram for intrinsic and extrinsic defects of different valence states for Ce-doped anatase (with VB, CB, E_g , and E_f for 0.10 mol% Ce) based on spin-polarised DFT calculations from others^{58,126,128,132} and from the present work: Ce_{Ti}^{\bullet} , $Ce_{Ti}^{\bullet\bullet}$, $Ce_{Ti}^{X(4+)}$ and $3+$, $Ce_i^{\bullet\bullet\bullet}$, and $Ce_i^{\bullet\bullet\bullet\bullet}$; E_g (from UV-Vis); VBM (from XPS valence XPS); CBM (from UV-Vis and valence XPS); and $E_f = 0.23$ eV (from AM-KPFM) versus normal hydrogen electrode (NHE); other reported E_f values are for samples processed under different conditions, where OA = oxidised and anhydrous, OH = oxidised and hydrated, RA = reduced and anhydrous, RH = reduced and hydrated, and SA = stoichiometric and anhydrous.¹³¹

as Ce_{Ti}^{\bullet} and $Ce_i^{\bullet\bullet}$. When these defects are close to the CB and so are n-type or close to the VB and so are p-type, they represent shallow energy levels (upper and lower one thirds of the band gap,¹²⁷ which act as electron donors or acceptors, respectively) and are likely to enhance charge carrier separation by promoting diffusion of charge carriers to the surface.^{35,61,62,128,129} When these defects are deep energy levels (which conventionally are viewed as being in the central one third of the band gap,¹³⁰ although this is viewed as a simplification¹²⁷), they also can act as electron donors or acceptors and so cause n- or p-type semiconductivity; however, these defects are likely to act as recombination centres for charge carriers and so would be unlikely to have the potential to enhance the photocatalytic performance.

Another important consideration for the defects revealed in Fig. 1 is the locations of their energy levels relative to the E_f . At 0 K, the theoretical E_f is defined as being in the middle of the band gap;⁶³ there do not appear to be any calculated values for the E_f at ambient conditions. However, at room temperature and in air, a representative value (*viz.*, E_f (OH)) for anatase is in the range 0.43 to 0.52 eV.¹³¹ The experimental E_f of 0.23 eV for 0.10 mol% Ce-doped TiO_2 from the present work was obtained from AM-KPFM data, as shown in Fig. XII (see ESI †).

As mentioned previously, for n-type semiconductors, such as anatase,^{58,132,133} the subshell energy levels likely to be available to electrons (since they have a 50% chance of being unfilled) are those that lie above the E_f ⁶⁴ (or below for p-type semiconductors). The relative locations of the experimental E_f ranges¹³¹ and midgap defect energies in Fig. 1 show that oxidising conditions during processing are desirable but that the inevitable presence of water vapour in the atmosphere during application is undesirable.

Examination of Fig. 1 reveals that, in relative order of energy level, the most important shallow midgap state defects for anatase are Ti_i^{\bullet} , Ce_{Ti}^{\bullet} , $Ce_{Ti}^{X(4+)}$, $Ce_{Ti}^{\bullet\bullet}$, O_i^{\bullet} , V_O^{\bullet} , $Ti_i^{\bullet\bullet}$, Ce_i^{\bullet} , $Ce_{Ti}^{X(3+)}$, $Ti_i^{\bullet\bullet\bullet}$, $V_O^{\bullet\bullet}$, and $Ce_i^{\bullet\bullet}$. However, since many of these are thermodynamically unfavourable owing to the significant changes from the common valence states (*viz.*, Ti_i^{\bullet} , V_O^{\bullet} , $Ti_i^{\bullet\bullet}$, Ce_i^{\bullet} and $Ce_i^{\bullet\bullet}$) or structural stability limitations (*viz.*, O_i^{\bullet}), then a practical assessment of the key shallow midgap states includes only Ce_{Ti}^{\bullet} , $Ce_{Ti}^{X(4+)}$, and $Ce_{Ti}^{\bullet\bullet}$. Although the neutral defect $Ce_{Ti}^{X(4+)}$ does not act as donor or acceptor, it can affect the mobilities of the charge carriers because it acts as a scattering centre.^{134,154} Of the other two key defects, Ce_{Ti}^{\bullet} lies well above the E_f and $Ce_{Ti}^{\bullet\bullet}$ lies slightly below the E_f . Consequently, these latter observations allow the conclusion that these defects are the only two relevant midgap state defects and that Ce_{Ti}^{\bullet} is favourably positioned and $Ce_{Ti}^{\bullet\bullet}$ is less favourably positioned to reduce the E_g . However, the proximity of both of these energy levels to the E_f indicates that both offer good chances of enhancing the semiconductivity by these means.

Reference to the new formalism for defect equilibria for the uncompensated stoichiometry described in eqn (24)–(43), summarised in Table 5 for anatase, reveals the Equations describing the relevant defect equilibria for the two key midgap state defects Ce_{Ti}^{\bullet} and $Ce_{Ti}^{\bullet\bullet}$:

Since aliovalent oxides generally are ionically charge compensated,¹³⁵ then the two most important defect equilibria in increasing the semiconductivity are likely to be described by eqn (24) and (27). Further, since the present work reports the doping of TiO_2 by Ce^{3+} , then eqn (24) represents the most important defect equilibria.

The data in Fig. 1 reveal the potential applicability of the additional shallow donor defects $Ti_i^{\bullet\bullet\bullet}$ and $Ce_{Ti}^{X(3+)}$. Since Ti

Table 5 Summary of key defect equilibria

Defect present					
Ce'_{Ti}		Ce'_{Ti}			
Kröger–Vink	New formalism	Kröger–Vink	New formalism	Solid solubility mechanism	Charge compensation mechanism
Eqn (11)	Eqn (27)	Eqn (8)	Eqn (24)	Substitutional	Ionic
Eqn (15)	Eqn (31)	Eqn (12)	Eqn (28)	Substitutional	Electronic

cannot be used to dope Ti, the Kröger–Vink formalism cannot be used to introduce $Ti_i^{\bullet\bullet}$ as a defect. However, the modified formalism for defect equilibria for uncompensated stoichiometry allows $Ti_i^{\bullet\bullet}$ to be introduced through eqn (26), (27), (30), and (31). Mechanistically, the introduction of $Ti_i^{\bullet\bullet}$ can be achieved by: (1) Ce^{3+} substitution for majority lattice Ti^{4+} , short-distance migration of Ti^{4+} to an adjacent interstice, and IVCT and (2) Ce^{3+} substitution for minority lattice Ti^{3+} and short-distance migration of Ti^{3+} to an adjacent interstice. These migrations are likely to be energetically favourable because the distance between the central lattice site and adjacent interstice is considerably less than that between the central lattice site and grain boundary sinks. In contrast, Ce_{Ti}^x ($3+$), like Ce_{Ti}^x ($4+$) is a neutral defect and so is neither donor nor acceptor, affecting the charge-carrier mobilities by acting as a scattering centre.^{134,154} Although V_O^{\bullet} is a deep donor defect, it is an intrinsic defect in TiO_{2-x} should be considered. It can be introduced through eqn (8) using the Kröger–Vink formalism. However, V_O^{\bullet} cannot be introduced using the new formalism because ionic charge compensation with which it is associated is replaced by $Ti^{4+} \leftrightarrow Ti^{3+}$ redox.

3.3 Mechanisms

The defect structures and solubility mechanisms must be interpreted by conceptual analogy with *all* of the experimental data in terms of the nature of the TiO_6 elongated octahedron,^{33,69} which is illustrated in Fig. 2. The key structural features are the two large, interstitial, fivefold coordinated voids of radius 0.0782 nm, located adjacent to the central Ti ion.

While Hume-Rothery's size rules for substantial, *interstitial*, metallic, solid solubility^{91,136} indicates that the solute cation should be substantially smaller than the solvent cation, the presence of the two large interstices in this covalent-ionic ceramic structure would be expected to be a possible solubility mechanism. While the cations smaller than the interstices, which are in fivefold coordination, are Ti^{3+} and Ti^{4+} , these normally would not be considered solutes. However, as indicated previously, it would be energetically more favourable for the central Ti ions to move from their lattice sites to one of these interstices rather than diffuse to the surface when forced by cation–cation repulsion established upon interstitial solid solubility. While both Ce^{3+} and Ce^{4+} appear to be too large for interstitial solid solubility, sufficient *c* axis expansion would be able to accommodate them.

Hume-Rothery's size rule for substantial, *substitutional*, metallic, solid solubility requires the solute cation radius to be within 15% of that of the solvent cation.^{91,136}

Although Table 1 suggests that neither Ce^{3+} nor Ce^{4+} would be likely to substitute for Ti^{4+} , $Ti^{4+} \rightarrow Ti^{3+}$ redox would be possible because the size accommodation allowed for this is clear (8.7%). However, a more important consideration is that this covalent-ionic structure of anatase includes two large adjacent interstices, which effectively increase the available volume substantially, provided *a*–*b* plane and *c* axis alterations can accommodate the distortion. Since the subsequent GAXRD data demonstrate clearly that substantial Ce solubility occurs, then the disagreement with Hume-Rothery's rules can be attributed to that facts that the anatase lattice does not consist of a close-

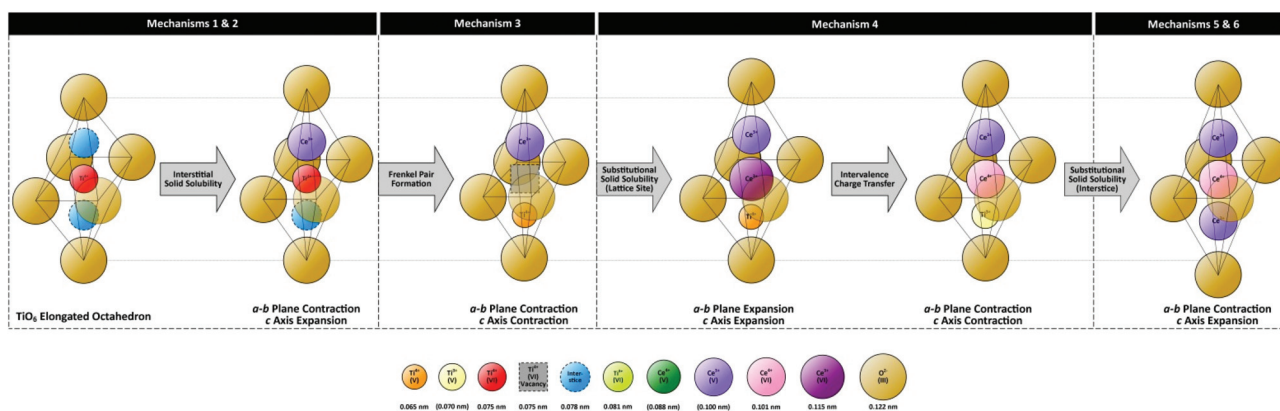


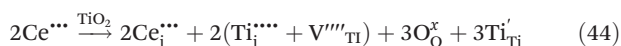
Fig. 2 Schematic of solubility mechanisms and resultant structural alteration of elongated TiO_6 octahedron in anatase.

packed metallic matrix, the volume of the combined central TiO_6 lattice site plus an adjacent interstice is very large, and oxygen vacancies may provide additional very large voids for interstitial solubility.

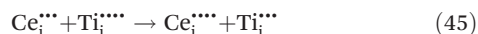
Another key point is that the anatase structure invariably is visualised in terms of only Ti^{4+} on the lattice sites, despite the known presence of minority Ti^{3+} . This has ramifications for the present work in terms of Hume Rothery's valence rules for both interstitial and substitutional solid solubilities,^{91,136} which indicate that solubility is favoured by similar valences. In effect, both interstitial solid solubility of Ce^{3+} and substitutional solid solubility to replace minority Ti^{3+} are feasible.

Correspondingly, interstitial solid solubility (Mechanisms 1–6) is shown in Fig. 2 in terms of dissolution Ce^{3+} , where 3+ is the valence of the Ce salt used for doping. This assumption is justified by the XPS data, which show that increased doping causes this valence's concentration to increase at a greater rate than that of Ce^{4+} . Also, the highly negatively charged environment of the fivefold interstice would favour retention of this environment by the presence of cations of lower valence. This assumption also is supported by the fact that, although doping commonly is considered to result in the formation of the thermodynamically most stable ion, regardless of the valence of the doping salt, this has been shown to be incorrect.¹³⁷

It is also possible that if Ce^{4+} were present, it dissolved but underwent $\text{Ce}^{4+} \rightarrow \text{Ce}^{3+}$ redox in the environment of the negatively charged interstice. This effectively would serve as a driving force for the IVCT mechanism given in eqn (2). When the relatively large Ce^{3+} ion (or the Ce^{4+} ion) is sited in the fivefold interstice (final stage of Mechanisms 1 & 2), repulsion with the Ti^{4+} ion causes the formation of a Frenkel defect, thereby transposing the Ti^{4+} ion from its sixfold lattice site into the remaining fivefold interstice, leaving behind a central vacancy (Mechanism 3), as shown in Fig. 2. As discussed for the new formalism for defect equilibria for uncompensated stoichiometry, this situation corresponds to that of eqn (32), which can be modified to accommodate the Frenkel defect formation:



As shown in Fig. 2, IVCT then would generate the reaction of eqn (45):



Charge compensation for the introduction of the dopant in eqn (44) is achieved through $\text{Ti}^{4+} \rightarrow \text{Ti}^{3+}$ redox on a lattice site (Ti'_{Ti}) and/or an interstitial site ($\text{Ti}'_{\text{Ti-i}}$). However, these redox reactions may be supplanted by IVCT. With the cations Ce^{3+} and Ti^{4+} in interstitial solid solution, these ionic shifts would be likely to result in a - b plane contraction (from the central vacancy) and c axis contraction (from the central vacancy and increased attraction between the interstitial ions and their fivefold-coordinating oxygen ions). Alternatively, c axis expansion could result from simple size considerations (ignoring the vacancy) resulting from the presence of the interstitial ions.

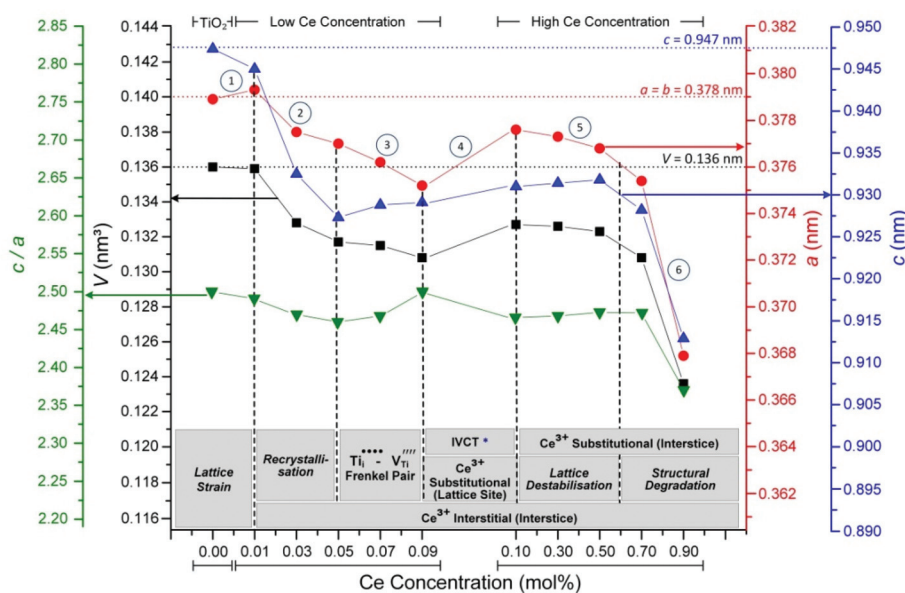
The c axis distortion would be asymmetric, thus effectively destabilising the structure. If IVCT occurs at this point, then this would reduce the asymmetry owing to size effects, where the Ce^{4+} and Ti^{3+} radii sizes of which would be closer to each other.

However, the XPS data in Tables III and IV (see ESI†) show that there are finite concentrations of Ti^{3+} , in which case Ce^{3+} substitutional solubility probably would be favoured owing to valence considerations. Here, the replacement of the Ti^{3+} by Ce^{3+} and resultant repulsion would transpose the former into the interstitial site. As discussed for the new formalism for defect equilibria for uncompensated stoichiometry, this situation corresponds to that of eqn (26).

However, it is likely that cation repulsion would shift the large Ce^{3+} off the lattice site, toward the remaining interstice, resulting in the partial occupancy of both lattice site and interstice by the Ce^{3+} , which has been referred to as *integrated solid solubility*.⁸⁹ With the cations Ce^{3+} and Ti^{3+} , the combination of matched valence and the positional compromise from integrated solid solubility would result in both a - b plane (where $a = b$) contraction (again from the central vacancy) and c axis contraction (again from the central vacancy and increased attraction between the interstitial ions and coordinating oxygen ions). However, again, c axis ions. Again, the c axis distortion would be asymmetric, thus effectively destabilising the structure, but the asymmetry expansion could result from the filling of the interstices by the would be reduced owing to the matched valences of the Ce^{3+} and Ti^{3+} interstitial ions.

The solubility of Ce in the anatase lattice is confirmed by the lattice parameters, the unit cell volumes, and c/a axial ratios, which are shown in Fig. 3. It also is confirmed by EDS, as shown in Fig. V (see ESI†). Examination the differential trends suggests that there are six, principal, staged, structural mechanisms that affect the crystal structure:

Mechanism 1 (0.00–0.01 mol% Ce). Upon initial doping, the conversion from a stable TiO_6 elongated octahedron to one subject to the dissolution of a large Ce^{3+} can be viewed in terms of an unstable situation involving the competing effects of initial dissolution, lattice strain, and relative destabilisation from structural distortion *versus* stabilisation from recrystallisation. Fig. 3 shows that initial doping causes the a - b plane to expand and the c axis to contract. The reduction in the c/a axial ratio suggests lattice contraction^{138,139} and this is supported by the Raman data in Fig. II (see ESI†), which show residual tensile stress from the shift to lower wavenumbers.¹⁴⁰ Consequently, any residual strain is likely to be small. The structural model in Fig. 2 shows that the solubility mechanism, which is interpreted in terms of interstitial solid solubility, should result in the converse effects of a - b plane contraction and c axis expansion. Although the contradiction may arise from differential surface and bulk effects, this is considered to be unlikely since the sol-gel method used can be considered to generate a homogeneous precursor.⁸⁹ It is noted that the greater effect is in the c axis contraction (and the a axis scale is amplified), which is consistent with facilitated recrystallisation (*i.e.*, reduced volume) of the precursor owing



Kröger-Vink	Ce'_{Ti}	$\text{Ce}^{\times}_{\text{Ti}} (3+)$	$\text{Ce}^{\times}_{\text{Ti}} (4+)$	$\text{Ce}^{\bullet\bullet}$
Description	Ce^{3+} Substitutional (Lattice Site)	Ce^{3+} Substitutional (Interstice)	Ce^{4+} Substitutional (Lattice Site)	Ce^{3+} Interstitial (Interstice)

Fig. 3 Graphical Rietveld analytical data for undoped and Ce-doped TiO_2 thin films with low (0.01–0.09 mol%) and high (0.10–0.90 mol%) Ce-doping concentrations, annealed at 450 °C for 2 h.

to the nucleating effect of the Ce solutes.¹⁴¹ In contrast, the simultaneous reduced extent of covalently bonded a - b plane expansion compared to c axis contraction is likely to be a response to the reduced repulsion caused by larger c axis contraction.

Mechanism 2 (0.01–0.05 mol% Ce). Fig. 3 shows that the low Ce-doping concentrations enhance more general recrystallisation (*i.e.*, reduced volume), which is reflected in contractions in both the c axis and a - b plane. Again, the c/a axial ratio reduction suggests lattice contraction^{138,139} and this is supported by the Raman data in Fig. II (see ESI†), which show residual tension. In contrast, the model of Fig. 2 suggests a - b plane contraction and c axis expansion. This mechanism involves completion of the recrystallisation initiated during Mechanism 1 by Ce^{3+} institutional solid solubility. In agreement, Fig. I (GAXRD) and II (Raman) (see ESI†) confirm that all low doping concentrations are associated with increases in crystallinity. These data reflect the competing effects of recrystallisation *versus* lattice strain caused by the onset of dissolution as well as the structural distortion from the charge-compensating $\text{Ti}^{4+} \rightarrow \text{Ti}^{3+}$ redox according to eqn (32)–(37) and the associated $\sim 9\%$ expansion on nearby Ti lattice sites according to the crystal radii in Table 1. The consistent trends in the a - b plane and c axis shown in Fig. 3 support the conclusion that, as shown in Fig. 2, the solubility mechanism is interstitial solid solubility deriving from Ce^{3+} dissolution, thereby forming the deep midgap state $\text{Ce}^{\bullet\bullet}$, as shown in Fig. 1. This stage terminates with the completion of recrystallisation,

which has been facilitated by the presence of the nucleating defects in the form of the Ce solutes.

Mechanism 3 (0.05–0.09 mol% Ce). Fig. 3 reveals that the trend in a - b plane contraction is maintained but the trend in the c axis is reversed, commencing a consistent increase with further doping. In this case, the increase in the c/a axial ratio suggests lattice expansion^{138,139} and this is supported by the residual tension revealed in the Raman data in Fig. II (see ESI†). This reversal signals the completion of recrystallisation and the onset of consistent c axis expansion as a reflection of the dissolution of the dopants along this direction. This trend suggests that the size effects of the interstitial ions (which would be expected to cause c axis expansion) overcome the attractions to the fivefold-coordinating oxygen ions (which would be expected to cause c axis contraction). The continuance of a - b plane contraction indicates that this also is the response to interstitial solid solubility. That is, the repulsion along the c axis from the introduction of the Ce^{3+} ion in an interstice forces the central Ti^{4+} ion to shift to the empty interstice, which represents a Ti^{4+} Frenkel pair (although this transposition also may be thermally activated¹⁴²). This scenario is in agreement with the model of Fig. 2. Subsequent balancing of repulsive and attractive forces by integrated solid solubility⁸⁹ probably shifts both ions to intermediate locations between the interstices and central vacancy. The XPS data, which are discussed subsequently, show that the Ti concentration for Mechanisms 1–4 decreases, indicating that only part of the Ti^{4+} is involved in Frenkel pair formation; the balance must be

interpreted conventionally as diffusing out of the lattice. This will not change the defect mechanisms but it will the defect concentrations. Since this involves Mechanism 4, it indicates that the defect mechanisms overlap.

Mechanism 4 (0.09–0.10 mol% Ce). Fig. 3 shows clearly that this structural mechanism corresponds to the introduction of another phenomenon that results in maintenance in the rate of c axis expansion, an abrupt a - b plane expansion, and significant decrease in c/a axial ratio (owing to differential extents of change). These are consistent with the *initial stage* of the model shown in Fig. 2, in which a large Ce^{3+} is introduced to the central Ti site (which is a vacancy at this point) by what can be considered to be substitutional solid solubility on the central lattice site, thereby forming the shallow midgap state Ce_{Ti}^x , as shown in Fig. 1. This situation results in the relatively unstable and hence simultaneous presence of what can be considered Ce^{3+} substitutional, Ce^{3+} interstitial, and Ti^{4+} interstitial ions, all within the TiO_6 elongated octahedron along the c axis. Consequently, maintenance of the TiO_6 octahedron would impose a significant compressive stress along the c axis, hence the large c axis expansion; the large Ce^{3+} substitutional ion would cause transverse a - b plane expansion. The Raman data in Fig. II (see ESI†) show that this condition equates to nil net stress. In the *final stage* of the model, shown in Fig. 2, the proximity of the electron orbitals of these cations facilitates IVCT^{33,68,91} according to eqn (2) ($\text{Ti}^{4+} + \text{Ce}^{3+} \rightarrow \text{Ti}^{3+} + \text{Ce}^{4+}$), as shown by the XPS results of Fig. XI (see ESI†). This IVCT reduces constraint on the TiO_6 tetrahedron and hence increases structural stability through increased interionic proximity (Table 1: $[\text{Ti}^{4+} + \text{Ce}^{3+} = 0.065 \text{ nm} + 0.100 \text{ nm} = 0.165 \text{ nm}] \rightarrow [\text{Ti}^{3+} + \text{Ce}^{4+} = 0.070 \text{ nm} + 0.088 \text{ nm} = 0.158 \text{ nm}]$). IVCT (at 0.09 mol% Ce) thus is responsible for the formation of more defects, as shown in Fig. 1, consisting of the midgap state $\text{Ti}_i^{\bullet\bullet}$, which is at the borderline between shallow and deep, and the shallow neutral midgap state $\text{Ce}_{\text{Ti}}^x(4+)$, which also is a scattering centre for charge carriers. The model of Fig. 2, the decreased c/a axial ratio of Fig. 3, and the electronegativity data for the ions in Table 2 all indicate that IVCT should result in overall lattice contraction and hence residual tensile stress. However, Fig. II (see ESI†) reveals a distinct residual compressive stress. Also, this cannot be attributed to differential thermal expansion, where anatase has a significantly higher expansion at 450 °C (ref. 143) than does silica glass,¹⁴⁴ since the stress state at the doping level immediately preceding (0.09 mol% Ce) was nil, thereby negating this influence. This contradiction is indicative of the mechanism overlaps that shade the transitions between mechanisms. Consequently, it is concluded that the consistent residual compressive stresses for Mechanisms 4–6, indicated clearly in Fig. II (see ESI†) are consistent with the increasing c/a axial ratio that commences at the final stage of Mechanism 4. Further, the mechanism overlap extends to the retention of the critical Ce_{Ti}^x defect during both the initial and final stages of Mechanism 4.

Mechanism 5 (0.10–0.60 mol% Ce). As there are few options for further dissolution of Ce, the structural symmetry and stability of the TiO_6 elongated octahedron is enhanced by sub-

stitution by Ce^{3+} on the interstitial site occupied by Ti^{3+} , thereby forcing the latter out of the octahedron to the grain boundaries and removing the borderline midgap state $\text{Ti}_i^{\bullet\bullet}$. Although the c axis continues to expand, the a - b plane abruptly contracts but the c/a axial ratio remains effectively constant (thus reflecting a balance between the two distortions). Again, these are consistent with the model shown in Fig. 2. Critically, the effective loss of the TiO_6 octahedron (in favour of a Ce_3O_6 octahedron) as well as the size and valence imbalances and constraints due to this Ce overdoping initiate the onset of large-scale lattice destabilisation. The substitution of Ti^{3+} by Ce^{3+} in the interstice, which forms the borderline defect $\text{Ce}_{\text{Ti}}^x(3+)$, which effectively is substitutional solid solubility in the interstice, establishes a $\sim 43\%$ expansion according to the crystal radii in Table 1. This contributes significantly to the lattice destabilisation according to eqn (32)–(37).

Mechanism 6 (0.60–0.90 mol% Ce). The GAXRD and Raman data shown in Fig. I and II, respectively (see ESI†), demonstrate that the crystallinity is maximised at 0.09 and 0.10 mol% Ce, decreasing at higher levels. At ≥ 0.60 mol% Ce, the existing solutes consist of Ce^{4+} on the Ti lattice site and two Ce^{3+} in the interstitial sites, which progressively converts stable TiO_2 to the unstable form Ce_3O_2 . The overdoping and extent of solubility reach such an extent that the lattice destabilisation proceeds to structural degradation, thereby initiating structural collapse, which would facilitate significant changes in the concentrations and valences of all species.

3.4 XPS data

Fig. 4 and 5 show the XPS data for Ti and Ce. The data for Ti in Fig. 4 suggest that the dominant solid solubility mechanism throughout the full dopant range (0.01–0.90 mol% Ce) is interstitial Ce^{3+} , which causes a 27.9% site expansion (see Table 1). However, at 0.09 mol% Ce, the abrupt increase in lattice volume reflects the 54.4% site expansion from what is effectively substitutional solid solubility of Ce^{3+} to replace Ti^{4+} in the lattice site. The simultaneous presence of both interstitial

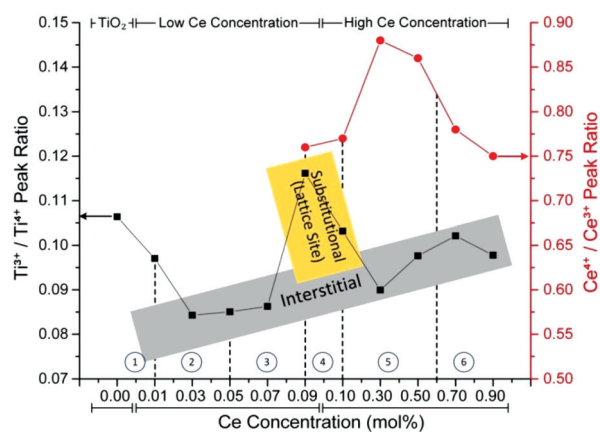


Fig. 4 Relative XPS data for undoped and Ce-doped TiO_2 thin films with low (0.01–0.09 mol%) and high (0.10–0.90 mol%) Ce-doping concentrations, annealed at 450 °C for 2 h.

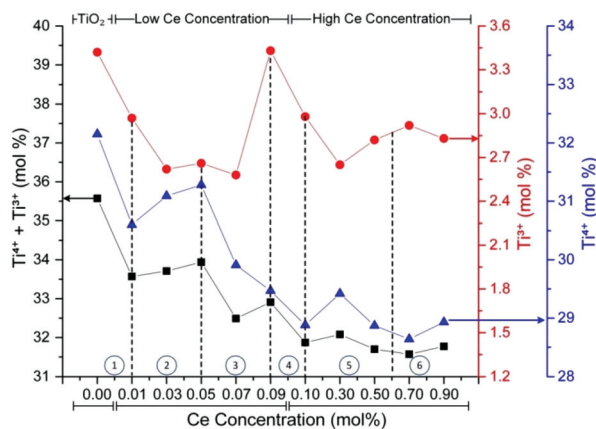


Fig. 5 XPS compensated data for undoped and Ce-doped TiO_2 thin films with low (0.01–0.09 mol%) and high (0.10–0.90 mol%) Ce-doping concentrations, annealed at 450 °C for 2 h.

and substitutional solid solubility has been observed before.^{145–148} This high-stress condition is mitigated by IVCT, as shown by the approximate converse (or mirror-image) trends of minority $[\text{Ti}^{3+}]$ and majority $[\text{Ti}^{4+}]$ in Fig. 5 as well as the converse trends for the data for the $\text{Ce}^{4+}/\text{Ce}^{3+}$ ratio (not detectable below concentration <0.09 mol% Ce) and $\text{Ti}^{3+}/\text{Ti}^{4+}$ ratio (until the highest Ce level, at which point the structure has degraded significantly) in Fig. 4.

Since IVCT, which occurs in the final stage of Mechanism 4, should result in mirror-image XPS data for Ti^{3+} and Ce^{4+} according to eqn (2), its effect can be seen for Mechanisms 5 and 6. The IVCT between Ti and Ce ions also is supported by the XPS data in Fig. VI–VIII and Tables III and IV (see ESI[†]), which are illustrated graphically in Fig. 5.

In Fig. 5, the gradual decreases in $[\text{Ti}^{3+}]$ and $[\text{Ti}^{4+}]$ are consistent with diffusion of Ti from the lattice. If this mechanism were conventional substitutional solid solubility, with Ce^{3+} replacing Ti^{4+} on the lattice site, then the Ce'_{Ti} defect would form. Since the significant effects of this defect at the doping level of 0.09–0.10 mol% Ce were not observed, then this mechanism is unlikely. Consequently, it is probable that the interstitial solid solubility of Ce^{3+} results in displacement of the central Ti^{4+} not only by Frenkel pair formation but also partly by removal from the TiO_6 octahedron and diffusion to the grain boundaries. Mechanism 5 also reveals gradual decreases in $[\text{Ti}^{3+}]$ and $[\text{Ti}^{4+}]$, which are consistent with the same process proposed previously. The slight increase in $[\text{Ti}^{3+}]$ and $[\text{Ti}^{4+}]$ in Mechanism 6 is suggestive of redissolution of grain boundary Ti upon structural destabilisation.

Fig. 6 shows that the crystallite size and the mean grain sizes from GAXRD, TEM, and AFM correlate well except for the AFM data, which generally consist of larger values and show a different trend for 0.01 to 0.05 mol% Ce doping concentration, as indicated in Fig. III and IV and Table II (see ESI[†]). These discrepancies probably resulted from the different nanostructures and measurement methods, where the AFM data recorded grain sizes across nonimpinging grains, thus inflat-

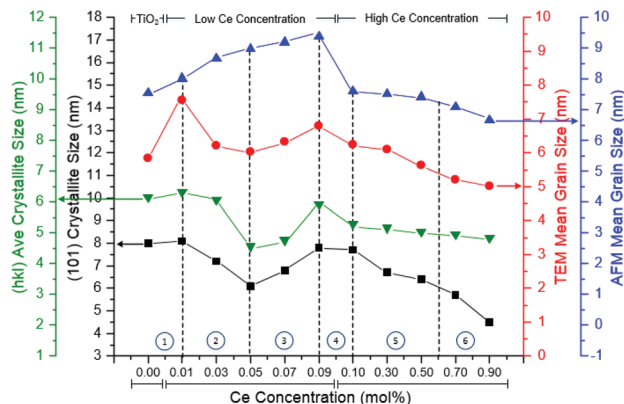


Fig. 6 Comparison between crystallite sizes from average crystallite size from all peaks (hkl) and main GAXRD peak (101) with mean grain sizes from TEM and AFM for undoped and Ce-doped TiO_2 thin films with low (0.01–0.09 mol%) and high (0.10–0.90 mol%) Ce-doping concentrations, annealed at 450 °C for 2 h.

ing the values, while the GAXRD and TEM data were effectively from direct measurements.

Fig. I (see ESI[†]) shows that the XRD peaks are relatively broad and of low intensity except for the (101) peak. Although the calculated crystallite sizes for the (hkl) average and (101) plane exhibit the same trends, deviation is clear in the high-Ce range, where lattice destabilisation and structural degradation, *i.e.*, amorphisation, occur. These data suggest that the crystallite sizes based on the (101) plane are more representative of the actual trend. Since TEM allows a direct visual assessment of grain size but AFM is an instrumental technique, the former is considered more reliable. Since the grain size is nearly identical to that of the crystallite size, it is clear that the grains are single crystal.

The changes in grain and crystallite sizes reinforce the different structural mechanisms identified in Fig. 3. However, it is noted that the data for Mechanism 4 in Fig. 6 reveal shrinkage while the equivalent data in Fig. 3 reveal lattice volume expansion. This is interpreted in terms of the effect of simultaneous occupancy of the central Ti^{4+} site by Ce^{3+} and of the interstices by Ce^{3+} and Ti^{4+} . Although IVCT would cause a subsequent contraction, net volume expansion would remain the case relative to Mechanism 3 owing to the integrated solid solubility enabled by the Ti vacancy. The presence of three cations in the TiO_6 elongated octahedron would cause significant lattice expansion and associated lattice destabilisation, which are reflected in the decreased intensities and broadening of the GAXRD peaks and Raman peaks in Fig. I and II, respectively (see ESI[†]). Consequently, this apparent contradiction in lattice expansion–contraction is an artefact of the onset of lattice destabilisation.¹⁴⁹

3.5 Energy band analysis

Fig. 7 shows the calculated band diagram for undoped and Ce-doped anatase using a range of data (see ESI[†]): optical indirect band gaps from UV-Vis spectrophotometry (Fig. IX and X

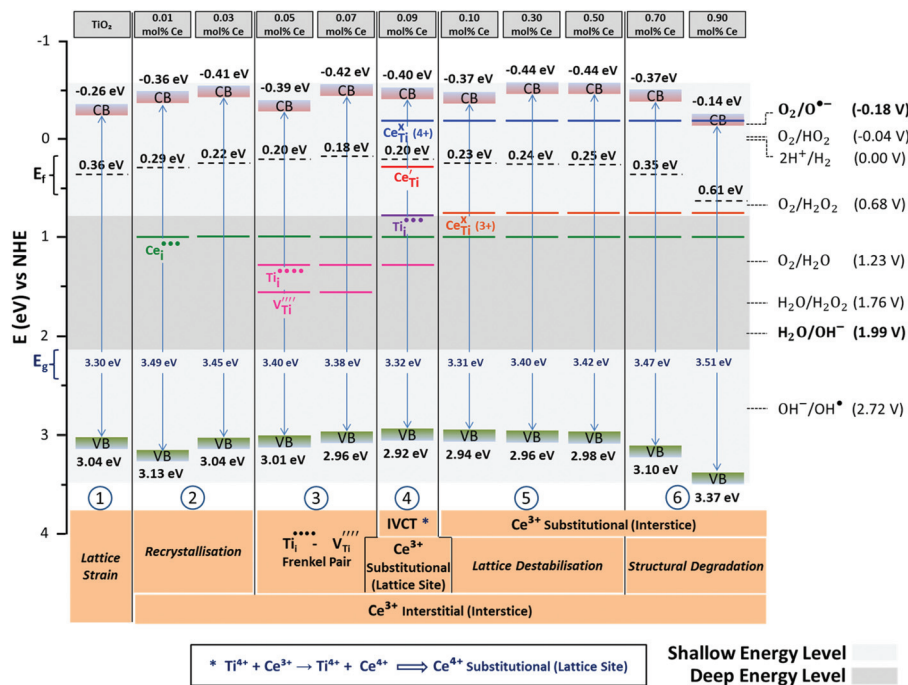


Fig. 7 Schematic energy band diagram: Midgap defect states indicated in Fig. 2 corresponding to the different mechanisms (bottom), positions of valence band (VB), conduction band (CB), and Fermi level (E_f) of undoped anatase TiO_2 and Ce-doped TiO_2 annealed at $450\text{ }^\circ\text{C}$ for 2 h (see Fig. 1 for origins of data).

and Table V_{Ti}^{\dagger}), VB spectra from XPS (Fig. XI \dagger), and the Fermi levels from AM-KPFM (Fig. XII \dagger). The midgap defect energy levels correspond to the defects indicated in Mechanisms 1–6 and shown in Fig. 2 and 3.

During Mechanisms 1–3, the increasing crystallinity and the dopant solubility increase the number of electrons (n_e), which has the effect of shifting the E_f from the VB toward the CB.¹⁵⁰ When the large Ce^{3+} ion substitutes for the small Ti^{4+} ion on the central lattice site (thus filling the $V_{\text{Ti}}^{\text{III}}$ and creating the defect Ce'_{Ti}), lattice destabilisation effectively commences, which lowers the E_f . Fig. 3 shows that, during the recrystallisation of Mechanism 2, both the a and c axes contract while, during the substitution of the small Ti^{3+} by the large Ce^{3+} in the interstice of Mechanism 5, the a axis contracts and the c axis expands, which suggests that this substitution initiates lattice destabilisation and hence the continued decrease in the E_f . Finally, the structural degradation of Mechanism 6 causes significant decreases in the E_f .

In amorphous (*viz.*, structurally degraded) materials, the E_f is located in what is known as the *mobility gap*, which is not a true band gap as in crystalline semiconductors.¹⁵⁰ The unsaturated bonds associated with the amorphised state represent defects that lie at the centre of the CB–VB gap and these can pin the Fermi level to the centre of the gap. This explains why Mechanism 6 is characterised by a decrease in the E_f toward the centre of the gap which is greater than the decreases of both the CB and VB.

The overall trend in the VB follows that of the E_f (except for Mechanism 1) because both depend on the n_e , where the VB

becomes more heavily populated as the E_g increases and hence the n_e decreases.¹⁵¹

In contrast, the ability of the electrons to bridge the E_g depends on the defects of midgap energy levels of suitable band positions, hence the variability of the CB locations.

Concerning the VB, at the low doping concentrations of Mechanisms 1–3, the decrease in E_g parallels the rise of the VB. The reason for this consistent trend results from the principal mechanism of interstitial solid solubility to increase the n_e . Eqn (44) shows that Frenkel pair formation in Mechanism 3, as shown in Fig. 2, requires the formation of the acceptor defect $V_{\text{Ti}}^{\text{III}}$, which, in principle, would raise the VB. When the mechanism of substitutional solid solubility on the Ti lattice site in the initial stage of Mechanism 4 introduces the shallow acceptor defect midgap state Ce'_{Ti} , the E_g is essentially at its minimal level, as shown in Fig. 8. However, Fig. 2 indicates that this defect is altered by IVCT in the final stage of Mechanism 4 to the neutral midgap state Ce^x_{Ti} . While this neutral defect is at a shallower level, as shown in Fig. 7, it would not contribute to alteration of the E_g because it acts as a scattering centre for charge carriers,^{134,154} as confirmed in Fig. 8. These considerations, which are limited to defect equilibria, suggest that the dominant defects are:

Mechanisms 1 and 2: Recrystallisation lowers the E_g .

Mechanism 3: The very deep midgap state $V_{\text{Ti}}^{\text{III}}$ lowers the E_g .

Mechanism 4: The shallow midgap state Ce'_{Ti} minimises the E_g (initial stage) but its effect is neutralised by IVCT (final stage).

Mechanisms 5 and 6: Lattice destabilisation and structural degradation raise the E_g .

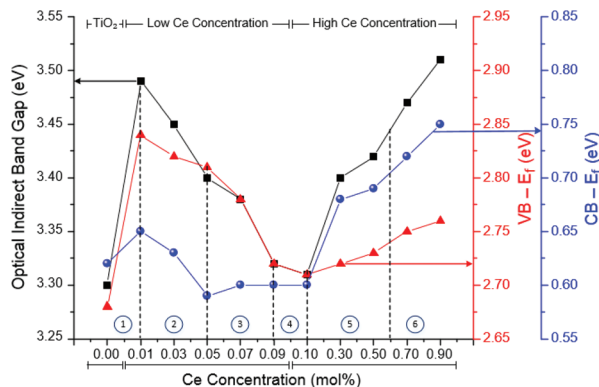


Fig. 8 Correlations between optical indirect band gap and valence band (VB) and conduction band (CB) positions for undoped and Ce-doped TiO_2 thin films with low (0.01–0.09 mol%) and high (0.10–0.90 mol%) Ce-doping concentrations, annealed at 450 °C for 2 h.

Concerning the CB, these data also show that, at the high doping concentrations of Mechanisms 5 and 6, there is increasing separation between the E_f and CB. Although the moderately deep defect $\text{Ce}_i^{\bullet\bullet}$ would be capable of lowering the CB, the trend of increasing separation between the E_f and CB is consistent with the lattice destabilisation and structural degradation associated with the conversion of TiO_2 to what effectively is Ce_3O_2 . Consequently, this extent of doping effectively represents donor overdoping, which involves occupation of higher CB states by dopant electrons. Overdoping causes the states within the conduction band to become filled, so the excited electrons must enter higher energy levels to enter the CB. This is known as the Moss-Burstein effect and it results in a blue shift in the optical absorption and consequent increase in the E_g .^{152–156} It is unlikely that overdoping caused semiconductor degeneracy because the maximal doping level is not consistent with defect densities orders of magnitude greater than those of the lower doping levels.¹⁵⁷

The overall trend in the E_g revealed by Fig. 8 is a reflection of the significant role played by changing crystallinity during doping, where recrystallisation at low doping concentrations enhance crystallinity and lower the E_g but lattice destabilisation and structural degradation cause amorphisation and raise the E_g . These effects have been observed many times before.^{33,91,158} These converse trends are reinforced by the effects of the residual lattice stress shown in the Raman data of Fig. II (see ESI†). At low and high doping concentrations, the peak shifts to lower and higher wave numbers, respectively, indicate residual tension and compression, respectively,¹⁵⁹ which generally are considered to lower and raise the E_g , respectively.¹³⁹ At the point at which the crystallinity is maximised and the residual stress is neutralised, the E_g is maximised by a significant amount relative to the two adjacent doping concentrations. This is attributed to the critical role of the shallow donor defect Ce_{Ti} as this is the only defect that is not a deep, acceptor, and/or scattering defect. Further, its energy level is slightly below the E_f , which is advantageous

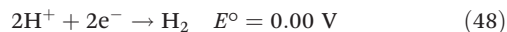
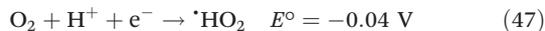
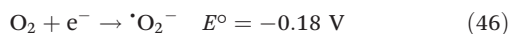
because, although ideally above the E_f for an n-type defect, its proximity still allows the n_c to equate to a relatively high concentration of electrons. However, the beneficial effect of the Ce_{Ti} defect in the initial stage of Mechanism 4 is negated by the elimination of this effect by IVCT in the final stage.

The effect of residual stress on the E_g has generated contradictory calculations in the literature. Yin *et al.*¹³⁹ considered uniaxial and hydrostatic tension and compression, concluding that compression increases the E_g . In contrast, Sun *et al.*¹³⁸ determined that uniaxial (c axis) compression causes a slight decrease in the E_g and biaxial (a – b plane) tension causes a significant decrease in the E_g . Interpretation of the data in Fig. 8 in terms of the mechanisms shown in Fig. 3 are complicated by the concurrent effects of partial amorphisation from initial doping (Mechanism 1), incomplete recrystallisation (Mechanism 2), and partial amorphisation from overdoping (Mechanisms 5 and 6), so only Mechanisms 3 and 4 are likely to reflect the unambiguous effects of strain on the E_g . In Mechanism 3, a – b plane contraction (biaxial compressive stress) and c axis expansion (uniaxial tensile stress) are accompanied by a significant decrease in the E_g . Thus, the present data are consistent with the model of Sun *et al.*¹³⁸ and so a – b plane strain effects would dominate the E_g . The defect equilibria include simultaneous $\text{Ce}_i^{\bullet\bullet}$ and $\text{Ti}_i^{\bullet\bullet\bullet} + \text{V}_{\text{Ti}}^{\bullet\bullet\bullet}$ Frenkel pair. Since Fig. 2 shows that the former is associated with c axis expansion but the latter is associated with c axis contraction, then the dominant effect on strain derives from the $\text{Ce}_i^{\bullet\bullet}$. Fig. 1 shows that $\text{Ce}_i^{\bullet\bullet}$, $\text{Ti}_i^{\bullet\bullet\bullet}$, and $\text{V}_{\text{Ti}}^{\bullet\bullet\bullet}$ are deep energy level defects, so they would be unlikely to affect the E_g . This discussion suggests that the E_g during Mechanism 3 is dominated by the strain and not the defect equilibria.

In Mechanism 4, the a – b plane expansion (biaxial tensile stress) and c axis expansion (uniaxial tensile stress) shown in Fig. 3 are accompanied by a small decrease in the E_g shown in Fig. 8. In this case, the former would decrease the E_g while the latter would increase it, suggesting that these opposing influences counter one another but that, in agreement with Sun *et al.*,¹³⁸ the a – b plane effect dominates that of the c axis. The defect considerations include Ce_{Ti} (initial stage) and IVCT (final stage). Since Fig. 2 shows that the former is associated with a – b plane and c axis expansions but the latter is associated with a – b plane and c axis contractions, then the dominant effect on strain would derive from centrally located Ce_{Ti} . The previous discussion of Mechanism 4 suggested that the onset and overlap of Mechanism 5 was responsible for the residual lattice compression in the final stage of Mechanism 4, hence the increased wavenumbers for Mechanisms 4–6 in Fig. II (see ESI†). Since residual compression should raise E_g ¹⁵⁹ but it is at a minimum, then this discussion suggests that the E_g during Mechanism 4 is dominated by the defect equilibria and not the strain.

The energy band diagram of Fig. 7 also includes a number of redox reactions that are important for water splitting from superoxide formation (eqn (46) and (47), bold in Fig. 7),^{160,161} hydrogen production (eqn (48)),¹⁶² and air purification by photocatalytic conversion of carbon dioxide into methane (eqn

(49))¹⁶³ as the position of the conduction band minimum (CBM) of anatase is above essentially all of the relevant redox potentials *versus* NHE at pH = 0.



3.6 Photocatalytic performance

Finally, Fig. 9 summarises the typical logarithmic¹⁵⁹ photocatalytic performance data, as shown in Fig. XIII (see ESI†). The former data correlate closely but inversely with the E_g data of Fig. 8, demonstrating that the photocatalytic performance of Ce-doped TiO₂ is dominated by the E_g . The shift in optimal performance from the initial stage to the final stage of Mechanism 4 (or to Mechanism 5 for 24 h) again is attributed to mechanism overlap. As discussed previously, the E_g in turn is dominated by crystallinity, residual stress, and the effect of the single shallow donor defect Ce'_{Ti}, which was present at the initial and final stages of Mechanism 4 at the doping concentration range of 0.09–0.10 mol% Ce. This doping concentration yielded the minimal E_g , highest VB, and second-highest E_f . A critical observation is the proximity of the energy level Ce'_{Ti} to the E_f , which effectively facilitates a source of electrons.

Fig. 10 contrasts the key data from the present work, revealing the following comparative characteristics:

Raman peak intensity. The correlation of the Raman peak intensity demonstrates that the structural regularity deriving from recrystallisation and lattice stabilisation contribute to the performance. These data also demonstrate that the partial amorphisation resulting from lattice destabilisation and struc-

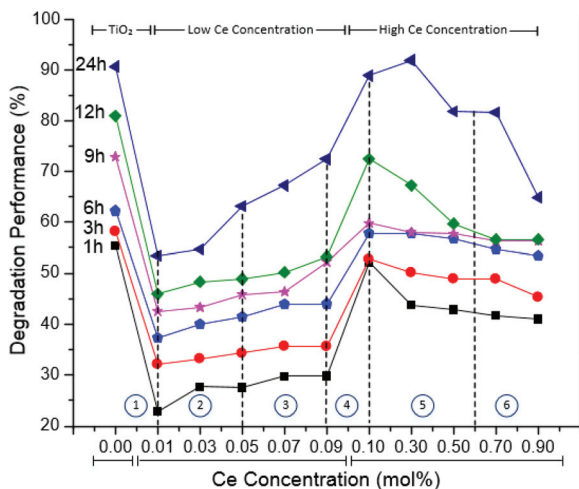


Fig. 9 Photodegradation of MB photocatalysed under UV light by undoped and Ce-doped TiO₂ thin films with low (0.01–0.09 mol%) and high (0.10–0.90 mol%) Ce-doping concentrations, annealed at 450 °C for 2 h.

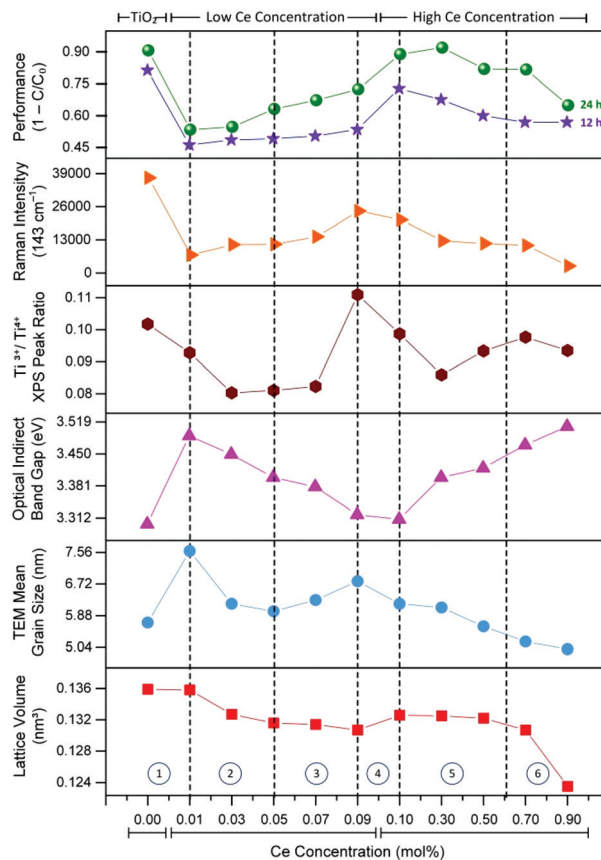


Fig. 10 Photodegradation performance of MB photocatalysed under UV light for 12 h or 24 h correlated with key data for low (0.01–0.09 mol%) and high (0.10–0.90 mol%) Ce-doping concentrations, annealed at 450 °C for 2 h.

tural destabilisation contribute to the degradation of the performance.

Ti³⁺/Ti⁴⁺ peak ratio. The maximum of [Ti³⁺] at the initial stage of Mechanism 4 suggests that this is a reflection of mechanism overlap and so the early onset of IVCT according to eqn (2). However, Ti³⁺ does not appear to contribute to the optimal photocatalytic performance since it is an acceptor defect and its defect energy level located it nearly as a deep defect. As it is a product of IVCT, it does not play a role in the formation of V_O[•] in the present analysis.

Optical indirect band gap. The inverse correlation of the E_g demonstrates that the decrease in the E_g resulting from the convergence of the CB and VB, increasing crystallinity, increasing residual tensile stress, and the effect of the single shallow donor defect Ce'_{Ti} contribute to the optimal performance at a doping concentration range of 0.09–0.10 mol% Ce.

TEM mean grain size. The inverse correlation of the grain size indicates that the maximal grain sizes of doped materials corresponded to the maximal performance, which is counter to the general expectation for the converse relation between grain size and surface area. Since Table II (see ESI†) does not reveal a correlation between roughness and photocatalytic performance, then this parameter does not appear to affect the

density of surface active sites. Further, the AFM and TEM data in Fig. II and III, respectively (see ESI†), indicate topographically similar surfaces. Consequently, these features do not appear to play a significant role in the performance.

Lattice volume. The similarly inverse correlation of the lattice volume supports the immediately preceding comments.

4. Conclusions

The present work reveals that band gap engineering through a carefully controlled regime of doping levels can be effective in the optimisation of the photocatalytic performance. However, the multiple defect mechanisms uncovered are considerably more nuanced than the general perception of the association of a single dopant with a single defect mechanism. Similarly, the present work reveals that the assumption of a single mechanism of solid solubility may be a simplification of considerably more complex processes. The acquisition of (1) a matrix of complementary characterisation and analytical data, (2) the calculation of a complete energy band diagram, including Fermi levels (3) consideration of uncompensated stoichiometry and charge compensation mechanisms beyond the limitations of Kröger–Vink approaches, (4) the development of a modified formalism for defect equilibria, and (5) the development of models of corresponding structural analogies establishes a new strategy for the interpretation and explanation of performance data. These strategies may allow one to deconstruct these complex issues and target optimal and possibly unique doping levels, thus potentially revealing experimental mechanisms for achieving lattice configurations that may be energetically and structurally unfavourable. These approaches then can be applied to other doped semiconducting systems.

In order to facilitate these strategies, a new formalism for defect equilibria, which is contrasted with the conventional Kröger–Vink notation, has been developed. This is based largely on the observation that most doping studies have been done based on the assumption that the stoichiometries during substitutional and interstitial solid solution as well as Schottky and Frenkel pair formation are *compensated* by diffusion of matrix ions to the grain boundaries or surface. In contrast, the new formalism is based on the assumption that stoichiometry is *uncompensated*. In this case, the central Ti in TiO₂ is transposed to an adjacent large interstitial site on the *c* axis and charge compensation is effected by Ti⁴⁺ → Ti³⁺ reduction of the central Ti.

These new approaches include the development of comprehensive defect energy level diagrams, generated by DFT simulations, which include all defects associated with majority Ti⁴⁺, minority Ti³⁺, Ce⁴⁺ dopant, and Ce³⁺ dopant. Many of the defect energy levels that have been calculated for Ce doping of TiO₂ appear to be the first to be reported. The generated diagrams include Fermi levels for both theoretical (at 0 K) and experimental (at 300 K) conditions.

The experimental data, all of which are mutually correlative, demonstrate that there are six progressive structural mecha-

nisms, which are illustrated by schematic models of the relevant processes. The initial solubility mechanism is interstitial involves dissolution of Ce³⁺ and subsequent formation of a Frenkel pair by transposition of the Ti⁴⁺ to the interstitial site and formation of a central Ti vacancy. The minimisation of size and valence imbalances probably occurs by integrated solid solubility. Crystallinity and lattice stress dominate the *E_g* during these mechanisms. At 0.09–0.10 mol% Ce, a substitutional solid solubility mechanism is activated, which significantly alters essentially all of the properties. This initial stage of this process involves occupation of the Ti lattice site by Ce³⁺ and the consequent introduction of the critical shallow donor defect Ce'_{Ti}. In the final stage of this process, IVCT (Ti⁴⁺ + Ce³⁺ → Ti³⁺ + Ce⁴⁺) occurs, eliminating Ce'_{Ti} and replacing it with the shallow neutral defect Ce_{Ti}^x. The defect equilibria dominate the *E_g* during this mechanism. At higher doping concentrations, a second substitutional solid solubility mechanism is activated, which involves Ce³⁺ substitution for Ti³⁺ in the interstice. This situation effectively leads to overdoping and deterioration of the structural integrity.

At the lowest doping concentration, the photocatalytic performance decreases significantly owing to the lattice destabilisation from the strain arising from initial doping (Mechanism 1). At the following low doping concentrations, the photocatalytic performance improves from a decrease in *E_g* due to increasing recrystallisation, residual tensile stress, interstitial solid solubility to raise the VB by increasing the *n_e*. (Mechanisms 2 and 3). At the middle doping concentrations of 0.09–0.10 mol%, the photocatalytic performance increases significantly owing to substitutional solid solubility on the lattice site. This creates the shallow donor defect Ce'_{Ti} (initial stage, Mechanism 4), which is located closely below the *E_f* and so enhances charge transfer. Its beneficial effect is diminished by its conversion to the shallow neutral defect Ce_{Ti}^x by IVCT, which acts as a scattering centre and so impedes charge transfer (final stage, Mechanism 4). At higher doping concentrations, the photocatalytic performance decreases owing partly to residual compressive stress. However, this is exacerbated by substitutional solid solubility in the interstice, the onset of amorphisation (Mechanism 5), and then structural collapse (Mechanism 6).

Conflicts of interest

There are no conflicts to declare.

Acknowledgements

The authors acknowledge the financial support of the Australian Research Council (ARC) (DP170104130), the UIPA Scholarship from UNSW Sydney Australia. The authors thank Dr Bin Gong and Dr Yin Yao for technical assistance and use of facilities at the Electron Microscope Unit within the Mark Wainwright Analytical Centre at UNSW Sydney.

References

- S. Bingham and W. A. Daoud, *J. Mater. Chem.*, 2011, **21**, 2041–2050.
- T. Tong, J. Zhang, B. Tian, F. Chen and D. He, *J. Hazard. Mater.*, 2008, **155**, 572–579.
- J. J. Douglas, M. J. Sevrin and C. R. Stephenson, *Org. Process Res. Dev.*, 2016, **20**, 1134–1147.
- R. Fagan, D. E. McCormack, D. D. Dionysiou and S. C. Pillai, *Mater. Sci. Semicond. Process.*, 2016, **42**, 2–14.
- M. Pelaez, N. T. Nolan, S. C. Pillai, M. K. Seery, P. Falaras, A. G. Kontos, P. S. Dunlop, J. W. Hamilton, J. A. Byrne and K. O'shea, *Appl. Catal., B*, 2012, **125**, 331–349.
- K. Nakata and A. Fujishima, *J. Photochem. Photobiol., C*, 2012, **13**, 169–189.
- B. Liu, Y. Fang, Z. Li and S. Xu, *J. Nanosci. Nanotechnol.*, 2015, **15**, 889–920.
- A. Fujishima, T. N. Rao and D. A. Tryk, *Electrochim. Acta*, 1999, **45**, 4683–4690.
- N. Alenzi, W. S. Liao, P. S. Cremer, V. Sanchez-Torres, T. K. Wood, C. Ehlig-Economides and Z. Cheng, *Int. J. Hydrogen Energy*, 2010, **35**, 11768–11775.
- C. H. Liao, C. W. Huang and J. Wu, *Catalysts*, 2012, **2**, 490–516.
- R. Sasikala, A. Shirole, V. Sudarsan, T. Sakuntala, C. Sudakar, R. Naik and S. Bharadwaj, *Int. J. Hydrogen Energy*, 2009, **34**, 3621–3630.
- Z. Sun, M. Liang and J. Chen, *Acc. Chem. Res.*, 2015, **48**, 1541–1550.
- B. Roose, S. Pathak and U. Steiner, *Chem. Soc. Rev.*, 2015, **44**, 8326–8349.
- W. M. Campbell, A. K. Burrell, D. L. Officer and K. W. Jolley, *Coord. Chem. Rev.*, 2004, **248**, 1363–1379.
- A. Fujishima, T. N. Rao and D. A. Tryk, *J. Photochem. Photobiol., C*, 2000, **1**, 1–21.
- D. Chen, *Sol. Energy Mater. Sol. Cells*, 2001, **68**, 313–336.
- V. Binas, D. Venieri, D. Kotzias and G. Kiriakidis, *J. Materiomics*, 2017, **3**, 3–16.
- H. Ren, P. Koshy, W. F. Chen, S. Qi and C. C. Sorrell, *J. Hazard. Mater.*, 2017, **325**, 340–366.
- D. Li, Q. Zhu, C. Han, Y. Yang, W. Jiang and Z. Zhang, *J. Hazard. Mater.*, 2015, **285**, 398–408.
- Y. Zhang, Z. Jiang, J. Huang, L. Y. Lim, W. Li, J. Deng, D. Gong, Y. Tang, Y. Lai and Z. Chen, *RSC Adv.*, 2015, **5**, 79479–79510.
- M. M. Mahlambi, C. J. Ngila and B. B. Mamba, *J. Nanomater.*, 2015, **2015**, 5.
- M. Muruganandham, R. P. Suri, M. Sillanpää, J. J. Wu, B. Ahmmad, S. Balachandran and M. Swaminathan, *J. Nanosci. Nanotechnol.*, 2014, **14**, 1898–1910.
- S. Banerjee, D. D. Dionysiou and S. C. Pillai, *Appl. Catal., B*, 2015, **176**, 396–428.
- J. Meng, P. Zhang, F. Zhang, H. Liu, J. Fan, X. Liu, G. Yang, L. Jiang and S. Wang, *ACS Nano*, 2015, **9**, 9284–9291.
- Y. Yao, Y. Ohko, Y. Sekiguchi, A. Fujishima and Y. Kubota, *J. Biomed. Mater. Res., Part B*, 2008, **85**, 453–460.
- R. Ameta and S. C. Ameta, *Photocatalysis: Principles and Applications*, CRC Press, Boca Raton FL, 2016.
- Z. Wang, E. Han, F. Liu and W. Ke, *J. Mater. Sci. Technol.*, 2007, **23**, 547–550.
- S. Aruna and G. Srinivas, *Surf. Eng.*, 2015, **31**, 708–713.
- H. M. A. El-Lateef and M. M. Khalaf, *Mater. Charact.*, 2015, **108**, 29–41.
- A. K. Braz, D. S. Moura, A. S. Gomes, T. Y. Ohulchanskyy, G. Chen, M. Liu, J. Damasco, R. E. de Araujo and P. N. Prasad, *J. Biophotonics*, 2018, **11**, DOI: 10.1002/jbio.201700029.
- Z. F. Yin, L. Wu, H. G. Yang and Y. H. Su, *Phys. Chem. Chem. Phys.*, 2013, **15**, 4844–4858.
- J. Rawat, S. Rana, M. Sorensson and R. Misra, *Mater. Sci. Technol.*, 2007, **23**, 97–102.
- W. F. Chen, P. Koshy, Y. Huang, E. Adabifiroozjaei, Y. Yao and C. C. Sorrell, *Int. J. Hydrogen Energy*, 2016, **41**, 19025–19056.
- M. Lin, H. Chen, W. Chen, A. Nakaruk, P. Koshy and C. Sorrell, *Int. J. Hydrogen Energy*, 2014, **39**, 21500–21511.
- S. Wang, L. Pan, J. J. Song, W. Mi, J. J. Zou, L. Wang and X. Zhang, *J. Am. Chem. Soc.*, 2015, **137**, 2975–2983.
- Y. Yamada and Y. Kanemitsu, *Appl. Phys. Lett.*, 2012, **101**, 133907.
- C. R. Kagan, E. Lifshitz, E. H. Sargent and D. V. Talapin, *Science*, 2016, **353**, DOI: 10.1126/science.aac5523.
- W. Kwong, N. Savvides and C. Sorrell, *Electrochim. Acta*, 2012, **75**, 371–380.
- S. H. Valencia Hurtado, J. M. Marín Sepúlveda and G. M. Restrepo Vásquez, *Open Mater. Sci. J.*, 2010, **4**, 9–14.
- T. Luttrell, S. Halpegamage, J. Tao, A. Kramer, E. Sutter and M. Batzill, *Sci. Rep.*, 2014, **4**, 4043.
- S. Valencia, J. M. Marín and G. Restrepo, *Open Mater. Sci. J.*, 2009, **4**, 9–14.
- K. Ozawa, M. Emori, S. Yamamoto, R. Yukawa, S. Yamamoto, R. Hobara, K. Fujikawa, H. Sakama and I. Matsuda, *J. Phys. Chem. Lett.*, 2014, **5**, 1953–1957.
- J. Moser, M. Grätzel and R. Gally, *Helv. Chim. Acta*, 1987, **70**, 1596–1604.
- W. Li, C. Ni, H. Lin, C. Huang and S. I. Shah, *J. Appl. Phys.*, 2004, **96**, 6663–6668.
- G. Liu, C. Y. Jimmy, G. Q. M. Lu and H. M. Cheng, *Chem. Commun.*, 2011, **47**, 6763–6783.
- C. V. Nguyen and N. N. Hieu, *Chem. Phys.*, 2016, **468**, 9–14.
- N. Lu, H. Guo, L. Li, J. Dai, L. Wang, W. N. Mei, X. Wu and X. C. Zeng, *Nanoscale*, 2014, **6**, 2879–2886.
- K. Zhao, Y. Wang, C. Xin, Y. Sui, X. Wang, Y. Wang, Z. Liu and B. Li, *Phys. Status Solidi B*, 2017, **254**, 82–87.
- A. Moridi, H. Ruan, L. Zhang and M. Liu, *Int. J. Solids Struct.*, 2013, **50**, 3562–3569.
- A. R. Albuquerque, A. Bruix, I. d. M. dos Santos, J. R. Sambrano and F. Illas, *J. Phys. Chem. C*, 2014, **118**, 9677–9689.

- 51 X. Wu, Z. Chen, G. Q. Lu and L. Wang, *Adv. Funct. Mater.*, 2011, **21**, 4167–4172.
- 52 U. Diebold, *Surf. Sci. Rep.*, 2003, **48**, 53–229.
- 53 X. Q. Gong and A. Selloni, *J. Phys. Chem. B*, 2005, **109**, 19560–19562.
- 54 N. Roy, Y. Park, Y. Sohn and D. Pradhan, *Semicond. Sci. Technol.*, 2015, **30**, 044005.
- 55 H. B. Jiang, Q. Cuan, C. Z. Wen, J. Xing, D. Wu, X. Q. Gong, C. Li and H. G. Yang, *Angew. Chem., Int. Ed.*, 2011, **50**, 3764–3768.
- 56 M. Liu, L. Piao, L. Zhao, S. Ju, Z. Yan, T. He, C. Zhou and W. Wang, *Chem. Commun.*, 2010, **46**, 1664–1666.
- 57 A. Ruiz Puigdollers, P. Schlexer, S. Tosoni and G. Pacchioni, *ACS Catal.*, 2017, **7**, 6493–6513.
- 58 J. Nowotny, M. A. Alim, T. Bak, M. A. Idris, M. Ionescu, K. Prince, M. Z. Sahdan, K. Sopian, M. A. M. Teridi and W. Sigmund, *Chem. Soc. Rev.*, 2015, **44**, 8424–8442.
- 59 H. Zhao, F. Pan and Y. Li, *J. Materiomics*, 2017, **3**, 17–32.
- 60 D. Hull and D. J. Bacon, *Introduction to Dislocations*, Butterworth-Heinemann, Oxford, 5th edn, 2011.
- 61 F. Amano, R. Tosaki, K. Sato and Y. Higuchi, *J. Solid State Chem.*, 2018, **258**, 79–85.
- 62 M. Nowotny, T. Bak and J. Nowotny, *J. Phys. Chem. B*, 2006, **110**, 16270–16282.
- 63 S. M. Sze and K. K. Ng, *Physics of Semiconductor Devices*, John Wiley & Sons, Hoboken, NJ, 3rd edn, 2006.
- 64 S. Sharma and P. K. Ahluwalia, *Eur. J. Phys.*, 2012, **33**, 883–895.
- 65 S. Shao, S. Wang, F. Jiang, H. Wu, T. Wu, Y. Lei, J. Fei and R. Koehn, *RSC Adv.*, 2016, **6**, 57722–57726.
- 66 L. G. Devi and R. Kavitha, *RSC Adv.*, 2014, **4**, 28265–28299.
- 67 D. A. Hanaor and C. C. Sorrell, *J. Mater. Sci.*, 2011, **46**, 855–874.
- 68 W. F. Chen, P. Koshy and C. C. Sorrell, *Int. J. Hydrogen Energy*, 2015, **40**, 16215–16229.
- 69 B. J. Morgan and G. W. Watson, *J. Phys. Chem. C*, 2010, **114**, 2321–2328.
- 70 S. S. Mofarah, E. Adabifiroozjahi, R. Pardehkorram, M. H. N. Assadi, M. Hinterstein, Y. Yao, X. Liu, M. B. Ghasemian, K. Kalantar-Zadeh, R. Mehmood, C. Cazorla, R. Shahmiri, G. Bahmanrokh, S. Bhattacharyya, M. C. Spadaro, J. Arbiol, S. Lim, Y. Xu, H. Arandiyani, J. Scott, P. Koshy and C. C. Sorrell, *Adv. Mater.*, 2019, DOI: 10.1002/adma.201905288.
- 71 L. Forro, O. Chauvet, D. Emin, L. Zuppiroli, H. Berger and F. Levy, *J. Appl. Phys.*, 1994, **75**, 633–635.
- 72 D. Liu, M. Zhang, W. Xie, L. Sun, Y. Chen and W. Lei, *Catal. Sci. Technol.*, 2016, **6**, 8309–8313.
- 73 M. Nolan, A. Iwaszuk, A. K. Lucid, J. J. Carey and M. Fronzi, *Adv. Mater.*, 2016, **28**, 5425–5446.
- 74 X. Li, H. Huang, H. Bin, Z. Peng, C. Zhu, L. Xue, Z. G. Zhang, Z. Zhang, H. Ade and Y. Li, *Chem. Mater.*, 2017, **29**, 10130–10138.
- 75 T. Jafari, E. Moharreri, A. S. Amin, R. Miao, W. Song and S. L. Suib, *Molecules*, 2016, **21**, DOI: 10.3390/molecules21070900.
- 76 R. Daghrir, P. Drogui and D. Robert, *Ind. Eng. Chem. Res.*, 2013, **52**, 3581–3599.
- 77 D. Tobaldi, A. S. Škapin, R. Pullar, M. Seabra and J. Labrincha, *Ceram. Int.*, 2013, **39**, 2619–2629.
- 78 V. Štengl, S. Bakardjieva and N. Murafa, *Mater. Chem. Phys.*, 2009, **114**, 217–226.
- 79 A. Zielińska-Jurek and J. Hupka, *Catal. Today*, 2014, **230**, 181–187.
- 80 T. Nogawa, T. Isobe, S. Matsushita and A. Nakajima, *Mater. Lett.*, 2012, **82**, 174–177.
- 81 R. R. Molinari, C. Lavorato and P. Argurio, *Chem. Eng. J.*, 2015, **274**, 307–316.
- 82 S. Sarina, E. R. Waclawik and H. Zhu, *Green Chem.*, 2013, **15**, 1814–1833.
- 83 T. Morikawa, R. Asahi, T. Ohwaki, K. Aoki and Y. Taga, *Jpn. J. Appl. Phys.*, 2001, **40**, 561–563.
- 84 A. E. R. Mohamed and S. Rohani, *Energy Environ. Sci.*, 2011, **4**, 1065–1086.
- 85 J. K. Zhou, L. Lv, J. Yu, H. L. Li, P. Z. Guo, H. Sun and X. Zhao, *J. Phys. Chem. C*, 2008, **112**, 5316–5321.
- 86 Q. Z. Yan, X. T. Su, Z. Y. Huang and C. C. Ge, *J. Eur. Ceram. Soc.*, 2006, **26**, 915–921.
- 87 J. J. Schneider, M. Matsuoka, M. Takeuchi, J. Zhang, Y. Horiuchi, M. Anpo and D. Bahnemann, *Chem. Rev.*, 2014, **114**, 9919–9986.
- 88 A. Yusov and V. Shilov, *Russ. Chem. Bull.*, 2000, **49**, 1925–1953.
- 89 W. F. Chen, S. S. Mofarah, D. A. H. Hanaor, P. Koshy, H. K. Chen, Y. Jiang and C. C. Sorrell, *Inorg. Chem.*, 2018, **57**, 7279–7289.
- 90 D. A. Atwood, *Sustainable Inorganic Chemistry*, John Wiley & Sons, Chichester, West Sussex, 2016, pp. 385–451.
- 91 W. F. Chen, H. Chen, P. Koshy, A. Nakaruk and C. C. Sorrell, *Mater. Chem. Phys.*, 2018, **205**, 334–346.
- 92 R. D. Shannon, *Acta Crystallogr., Sect. A: Cryst. Phys., Diffraction, Theor. Gen. Crystallogr.*, 1976, **32**, 751–767.
- 93 M. Martos, B. Julián-López, J. V. Folgado, E. Cordoncillo and P. Escribano, *Eur. J. Inorg. Chem.*, 2008, **2008**, 3163–3171.
- 94 G. W. Wicks, *The Handbook of Photonics*, ed. M. C. Gupta and J. Ballato, CRC Press, Boca Raton, FL, 2nd edn, 2018, pp. 1–19.
- 95 B. Gong, X. Luo, N. Bao, J. Ding, S. Li and J. Yi, *Surf. Interface Anal.*, 2014, **46**, 1043–1046.
- 96 D. W. Smith, *J. Chem. Educ.*, 1990, **67**, 911.
- 97 L. Chung, W. F. Chen, P. Koshy and C. C. Sorrell, *Mater. Chem. Phys.*, 2017, **197**, 236–239.
- 98 M. Ni, M. K. Leung, D. Y. Leung and K. Sumathy, *Renewable Sustainable Energy Rev.*, 2007, **11**, 401–425.
- 99 L. C. Allen, *J. Am. Chem. Soc.*, 1989, **111**, 9003–9014.
- 100 A. L. Allred and E. G. Rochow, *J. Inorg. Nucl. Chem.*, 1958, **5**, 264–268.
- 101 E. J. Little Jr. and M. M. Jones, *J. Chem. Educ.*, 1960, **37**, 231.
- 102 M. V. Putz, N. Russo and E. Sicilia, *Theor. Chem. Acc.*, 2005, **114**, 38–45.

- 103 J. C. Boeyens, *Z. Naturforsch., B: J. Chem. Sci.*, 2008, **63**, 199–209.
- 104 L. Pauling, *J. Am. Chem. Soc.*, 1932, **54**, 3570–3582.
- 105 R. G. Pearson, *Inorg. Chem.*, 1988, **27**, 734–740.
- 106 R. T. Sanderson, *J. Am. Chem. Soc.*, 1983, **105**, 2259–2261.
- 107 K. Li and D. Xue, *J. Phys. Chem. A*, 2006, **110**, 11332–11337.
- 108 J. K. Nagle, *J. Am. Chem. Soc.*, 1990, **112**, 4741–4747.
- 109 F. Kröger and H. Vink, in *Solid state physics*, Elsevier, 1956, vol. 3, pp. 307–435.
- 110 J. Zhang, W. Peng, Z. Chen, H. Chen and L. Han, *J. Phys. Chem. C*, 2012, **116**, 19182–19190.
- 111 T. Marimuthu, N. Anandhan, S. Rajendran, M. Mummooorthy and M. Vidhya, *Int. J. ChemTech Res.*, 2014, **6**, 5309–5314.
- 112 M. Popa, E. Indrea, P. Pascuta, V. Cosoveanu, I. C. Popescu and V. Danciu, *Rev. Roum. Chim.*, 2010, **55**, 369–375.
- 113 G. Li, D. Zhang and C. Y. Jimmy, *Phys. Chem. Chem. Phys.*, 2009, **11**, 3775–3782.
- 114 W. Xue, G. Zhang, X. Xu, X. Yang, C. Liu and Y. Xu, *Chem. Eng. J.*, 2011, **167**, 397–402.
- 115 M. Sidheswaran and L. L. Tavlarides, *Ind. Eng. Chem. Res.*, 2009, **48**, 10292–10306.
- 116 C. Wang, Y. Ao, P. Wang, J. Hou, J. Qian and S. Zhang, *J. Hazard. Mater.*, 2010, **178**, 517–521.
- 117 C. Fan, P. Xue and Y. Sun, *J. Rare Earths*, 2006, **24**, 309–313.
- 118 G. Magesh, B. Viswanathan, R. Viswanath and T. Varadarajan, *Indian J. Chem.*, 2009, **48**, 480–488.
- 119 A. Vincent, *Oxidation and Reduction in Inorganic and Analytical Chemistry: A Programmed Introduction*, John Wiley & Sons Inc, New York, 1985.
- 120 Standard reduction potentials, <https://www.av8n.com/physics/redpot.htm> (accessed October 2018).
- 121 W. M. Haynes, *CRC Handbook of Chemistry and Physics*, CRC Press, New York, 96th edn, 2015.
- 122 J. Rumble, *CRC Handbook of Chemistry and Physics*, CRC Press, New York, 98th edn, 2017.
- 123 C. Guang-Sen, M. Okido and T. Oki, *Electrochim. Acta*, 1987, **32**, 1637–1642.
- 124 A. Dicks and D. A. J. Rand, *Fuel Cell Systems Explained*, John Wiley & Sons, Chichester, West Sussex, 3rd edn, 2018.
- 125 F. Pan and Q. Wang, *Molecules*, 2015, **20**, 20499–20517.
- 126 J. He, R. Behera, M. Finnis, X. Li, E. Dickey, S. Phillpot and S. B. Sinnott, *Acta Mater.*, 2007, **55**, 4325–4337.
- 127 H. J. Queisser and E. E. Haller, *Science*, 1998, **281**, 945–950.
- 128 Q. Wang, Z. Zhang, S. M. Zakeeruddin and M. Grätzel, *J. Phys. Chem. C*, 2008, **112**, 7084–7092.
- 129 J. Weidmann, T. Dittrich, E. Konstantinova, I. Laueremann, I. Uhlendorf and F. Koch, *Sol. Energy Mater. Sol. Cells*, 1999, **56**, 153–165.
- 130 A. Ramdas and S. Rodriguez, *Rep. Prog. Phys.*, 1981, **44**, 1297.
- 131 S. Kashiwaya, J. Morasch, V. Streibel, T. Toupance, W. Jaegermann and A. Klein, *Surfaces*, 2018, **1**, 73–89.
- 132 A. R. Albuquerque, A. Bruix, J. R. Sambrano and F. Illas, *J. Phys. Chem. C*, 2015, **119**, 4805–4816.
- 133 J. Nowotny, *Energy Environ. Sci.*, 2008, **1**, 565–572.
- 134 D. Redfield and R. H. Bube, *Photo-Induced Defects in Semiconductors*, Cambridge University Press, Cambridge, 1996.
- 135 Y. M. Chiang, D. P. Birnie, W. D. Kingery and S. Newcomb, *Physical Ceramics: Principles for Ceramic Science and Engineering*, Wiley New York, 1997.
- 136 W. Hume-Rothery, R. E. Smallman and C. W. Haworth, *The structure of metals and alloys*, The Institute of Metals, The Metals and Metallurgy Trust of the Institute of Metals and the Institution of Metallurgists, London, 5th edn, 1969.
- 137 Z. Liu, W. F. Chen, X. Zhang, J. Zhang, P. Koshy and C. C. Sorrell, *J. Phys. Chem. C*, 2019, **18**, 11781–11790.
- 138 Y. Sun, S. Thompson and T. Nishida, *J. Appl. Phys.*, 2007, **101**, DOI: 10.1063/1.2730561.
- 139 W. J. Yin, S. Chen, J. H. Yang, X. G. Gong, Y. Yan and S. H. Wei, *Appl. Phys. Lett.*, 2010, **96**, DOI: 10.1063/1.3430005.
- 140 G. Parsard, G. Subhash and P. Jannotti, *J. Am. Ceram. Soc.*, 2018, **101**, 2606–2615.
- 141 W. D. Kingery, H. K. Bowen and D. R. Uhlmann, *Introduction to Ceramics*, John Wiley & Sons, New York, 2nd edn, 1976.
- 142 K. Funke, D. Wilmer, T. Lauxtermann, R. Holzgreve and S. Bennington, *Solid State Ionics*, 1996, **86**, 141–146.
- 143 K. K. Rao, S. N. Naidu and L. Iyengar, *J. Am. Ceram. Soc.*, 1970, **53**, 124–126.
- 144 E. B. Shand, *Glass Engineering Handbook, 2nd Edition*, McGraw-Hill Book Company, New York, 1958, (33 pp).
- 145 J. F. Stebbins, *Chem. Mater.*, 2007, **19**, 1862–1869.
- 146 H. Rücker, B. Heinemann, W. Röpkke, R. Kurps, D. Krüger, G. Lippert and H. Osten, *Appl. Phys. Lett.*, 1998, **73**, 1682–1684.
- 147 A. Magerl, J. Rush, J. Rowe, D. Richter and H. Wipf, *Phys. Rev. B: Condens. Matter Mater. Phys.*, 1983, **27**, 927.
- 148 R. Hall and J. H. Racette, *J. Appl. Phys.*, 1964, **35**, 379–397.
- 149 U. Holzwarth and N. Gibson, *Nat. Nanotechnol.*, 2011, **6**, 534.
- 150 V. Ivashchenko, P. E. Turchi, S. Veprek, V. Shevchenko, J. Leszczynski, L. Gorb and F. Hill, *J. Appl. Phys.*, 2016, **119**, 205105.
- 151 J. H. Yang, W. J. Yin, J. S. Park and S. H. Wei, *Sci. Rep.*, 2015, **5**, 16977.
- 152 M. Öztas and M. Bedir, *Thin Solid Films*, 2008, **516**, 1703–1709.
- 153 T. Tansley and C. Foley, *J. Appl. Phys.*, 1986, **59**, 3241–3244.
- 154 S. Snega, K. Ravichandran, M. Baneto and S. Vijayakumar, *J. Mater. Sci. Technol.*, 2015, **31**, 759–765.
- 155 M. Rychetsky, I. Koslow, T. Wernicke, J. Rass, V. Hoffmann, M. Weyers and M. Kneissl, *Phys. Status Solidi B*, 2016, **253**, 169–173.
- 156 K. Sivula and R. Van De Krol, *Nat. Rev. Mater.*, 2016, **1**, 15010.

- 157 F. Poupaud and C. Schmeiser, *Math. Methods Appl. Sci.*, 1991, **14**, 301–318.
- 158 T. S. Sakthivel, D. L. Reid, U. M. Bhatta, G. Möbus, D. C. Sayle and S. Seal, *Nanoscale*, 2015, **7**, 5169–5177.
- 159 K. Maeda, *ACS Catal.*, 2013, **3**, 1486–1503.
- 160 C. E. Diaz-Uribe, M. C. Daza, F. Martínez, E. A. Páez-Mozo, C. L. Guedes and E. Di Mauro, *J. Photochem. Photobiol., A*, 2010, **215**, 172–178.
- 161 S. Wang, J. H. Yun, B. Luo, T. Butburee, P. Peerakiatkhajohn, S. Thaweesak, M. Xiao and L. Wang, *J. Mater. Sci. Technol.*, 2017, **33**, 1–22.
- 162 D. J. Martin, in *Investigation into High Efficiency Visible Light Photocatalysts for Water Reduction and Oxidation*, Springer, 2015, pp. 1–53.
- 163 A. Cybula, M. Klein and A. Zaleska, *Appl. Catal., B*, 2015, **164**, 433–442.